Advanced Science

ADVANCED SCIENCE Open Access

www.advancedscience.com

RESEARCH ARTICLE OPEN ACCESS

Studying Macromolecular Composition in Cell–Cell Interfaces Using 3D Membrane Reconstitution Systems

Franziska Ragaller[1] | Amelie Maribel Schneider[1] | Ellen Sjule[1] | Renhua Sun[2] | Xiao Han[2] | Luca Andronico[1] | Edward Jenkins[3] | Michael Dustin[3] | Adnane Achour[2] | Erdinc Sezgin[1]

[1]Science for Life Laboratory, Department of Women's and Children's Health, Karolinska Institutet, Solna, Sweden | [2]Science for Life Laboratory, Department of Medicine, Karolinska Institute & Division of Infectious Diseases, Karolinska University Hospital, Solna, Sweden | [3]Kennedy Institute of Rheumatology, NDORMS, University of Oxford, Oxford, UK

Correspondence: Franziska Ragaller (franziska.ragaller@ki.se) | Erdinc Sezgin (erdinc.sezgin@ki.se)

Received: 6 November 2025 | **Revised:** 11 March 2026 | **Accepted:** 12 March 2026

ABSTRACT

During direct communication between two cells, the plasma membranes of each cell serve as a platform for ligand-receptor interaction initiating downstream signaling cascades. In immune cell signaling, this cell–cell interface – the immune synapse – is highly spatiotemporally organized. Multiple stimulatory and co-stimulatory signals need to be integrated over time to ensure proper immune cell function. This process is still not fully understood given the vast complexity of interactions between proteins, lipids, glycocalyx and associated cortical actin cytoskeleton. Here, we presented a fully artificial model system to study the interface between two vesicles and a semi-artificial one between a live cell and a vesicle to reconstitute 3D contacts. We investigated the distribution and reorganization of immune cell proteins at artificial and semi-artificial contacts. We show the enrichment and depletion of different proteins in the synapse and how different peptides with varying affinity presented by the same MHC class I affect T cell activation. We further explored the distribution of glycocalyx elements and showed differential partitioning of different sugar moieties in the interface. While we focused on the T cell interface here, our model systems are powerful tools to study the distribution and reorganization of lipids, proteins and glycocalyx components at any cell–cell contact.

1 | Introduction

Cell–cell communication is needed to react and adapt to environmental cues and thus crucial for the survival of multicellular organisms. To integrate external signals and mediate subsequent functions, highly sophisticated inter- and intracellular signaling networks have evolved [1]. Initial events in these signaling cascades occur at the plasma membrane, which not only serves as a platform for receptors and ligands to interact, but also influences the nature and dynamics of this interaction [2, 3].

In the context of immune cell signaling, a highly spatiotemporally organized contact is formed between immune cells and their target, called the immune synapse [4, 5]. The immune synapse, best described for T cells, is spatially organized in supramolecular activation clusters, characterized by abundance or exclusion of certain proteins [4]. For an immune cell to decide how and when to respond, multiple stimulatory and inhibitory signals need to be integrated over time [6, 7]. To fully understand this process, the role of individual components needs to be dissected in time and space. However, this is not trivial due to the complexity at the contact, including protein–protein interactions [4], lipid–protein interactions [8, 9], glycocalyx involvement [10], and cytoskeleton activity [11].

By facilitating the examination of individual components involved in immune cell interactions in a live-cell context, model membrane systems of controllable complexity have gained popularity. These model membrane systems allow control over lipid composition of the membrane and proteins

This is an open access article under the terms of the Creative Commons Attribution License, which permits use, distribution and reproduction in any medium, provided the original work is properly cited.

© 2026 The Author(s). *Advanced Science* published by Wiley-VCH GmbH

attached to functionalized lipids within the membrane. The use of supported lipid bilayers (SLB) on flat glass surfaces facilitated crucial advancements in our knowledge on immune cell interfaces and activation [12–16]. Further, SLBs allow for advanced imaging techniques such as total internal reflection fluorescence microscopy (TIRFM) and single-molecule localization microscopy (SMLM) [17]. However, the glass support impacts the diffusion behavior of lipids and attached proteins [18, 19] and increases the stiffness of the membrane beyond what immune cells typically encounter [20, 21]. Both T and B cells are highly sensitive to the stiffness of their substrate, with an increase in stiffness correlating to increased triggered signaling [22–28]. Additionally, using SLBs, the cell–cell interface can only be investigated in 2D; however, cells normally form a 3D contact [29]. These limitations can be overcome with the use of free-standing systems such as giant unilamellar vesicles (GUVs), allowing for reconstitution of 3D contacts closer to physiological conditions. GUVs can mimic cells well in terms of size, ranging from 1–100 μm in diameter, and also in flexibility, finite surface area, tension, deformability, and stiffness [30–32]. GUVs have previously been used to mimic immune cell interfaces in combination with themselves or SLBs [33, 34] and in combination with cell lines [35].

Built on these previous reconstitution systems, we have developed two widely applicable model systems to study cell–cell interfaces. We explored the formation of completely artificial contacts using only GUVs, as well as semi-artificial contacts using GUVs in combination with T cell lines or primary human $CD8^+$ T cells. We prepared GUVs by electroformation, comprising our lipids of choice and nitrilotriacetic acid (Ni-NTA)-functionalized lipids to attach His-tagged proteins to the GUV surface. We examined the distribution of adhesion molecules, T cell receptors (TCR) and peptide major histocompatibility complexes (pMHC), checkpoint inhibitors, and heavily glycosylated proteins at the artificial and semi-artificial contact. We further investigated ZAP70 recruitment and Ca^{2+} signaling as indicators for T cell activation in our semi-artificial model system using both confocal and lattice light-sheet microscopy as a function of peptide affinity to TCR. Finally, we explored the glycocalyx distribution at reconstituted immune cell interfaces using lectins with specificity for different sugar residues.

While we have mainly investigated the T cell contact, the model systems presented here can be applied to a wide range of cell–cell interactions. The feasibility and versatility of these model systems make them a powerful tool to study the distribution and reorganization of lipids, proteins and glycocalyx components at 3D cell–cell interfaces.

2 | Methods

2.1 | Materials

We used the following lipids and fluorescent lipid probes: 1-palmitoyl-2-oleoyl-glycero-3-phosphocholine (POPC, 16:0-18:1 PC), 1-palmitoyl-2-oleoyl-sn-glycero-3-phospho-L-serine (POPS, 16:0/18:1 PS), 1,2-dioleoyl-sn-glycero-3-[(N-(5-amino-1-carboxypentyl)iminodiacetic acid)succinyl] (nickel salt) (18:1 DGS-NTA (Ni)), 23-(dipyrrometheneboron difluoride)-24-norcholesterol (TopFluor Cholesterol), 1-palmitoyl-2-(dipyrromethene boron difluoride) undecanoyl-sn-glycero-3-phosphoethanolamine (TopFluor PE) (Avanti Polar Lipids), Abberior-STAR RED-PE (ASR-PE, Abberior GmbH) and NR12A [36].

We used the following recombinant proteins obtained from Sino Biological: human CD2 (His-Tag,10982-H08H), CD58/human LFA-3 (His-Tag, 12409-H08H), PD1/human PDCD1 (His-Tag,10377-H08H), PD-L1/human B7-H1/ CD274 (His-Tag, 10084-H08H), CD80/human B7-1 (His-Tag, 10698-H08H), human CTLA-4 (His-Tag,11159-H08H), NCR3/human NKp30 (His-Tag, 10480-H08H), human B7-H6 (His-Tag, 16140-H08H), human SLAMF6/human Ly108 (His-Tag, 11945-H08H), human CD84 (His-Tag, 10100-H08H), human SIRPαV2 (His-Tag, 30014-H08H), human CD47 (His-Tag, 12283-H08H), CD45 (ECD, His-Tag, 14197-H08H). We also used the proteins: CD43/ human leukosialin (His-Tag, CD3-H52H9, ACROBiosystems), MUC1-Alexa Fluor 488 (kindly provided by Carolyn Shurer), MHC class I H-$2D^b$ presenting the LCMV-derived gp33 peptide (KAVYNFATM) [37, 38], MHC class I (HLA-A*02:01) presenting the tumor-associated antigen NY-ESO1-9 V peptide (SLLMWITQV; from now on 9 V) [39], MHC class I (HLA-A*02:01) presenting the NY-ESO1-3P9V peptide variant (SLPMWITQV; from now on 3P9V), P14 TCR [38], 1G4 TCR [39], Wheat Germ Agglutinin (WGA) Alexa Fluor 647 Conjugate (ThermoFisherScientific), Aleuria Aurantia Lectin (AAL) (L-1390-2, Vector Labs), Sambucus Nigra-I-Agglutinin (SNA) (L-1300-5, Vector Labs), Maackia Amurensis-II Lectin (MAL-II) (L-1260-2, Vector Labs). We used Alexa Fluor 488 or 647 NHS Ester (Succinimidyl Ester) (ThermoFisher Scientific) for protein labeling.

NaCl, HEPES and CaCl2 were obtained from Sigma-Aldrich (St. Louis, MO, USA). Gibco PBS, RPMI (with L-glutamine), fetal bovine serum (FBS), Gibco L-glutamine (200 mM,100x), Gibco sodium pyruvate (100 mM), Gibco MEM non-essential amino acids solution (100x), Gibco HEPES buffer solution (1 M, 100x), Gibco Leibovitz's L-15 Medium (no phenol red) and Cytiva Ficoll-Paque PLUS Media were obtained from ThermoFisher Scientific. Recombinant human IL-2 protein was obtained from BioTechne. Fluo-4, AM was obtained from ThermoFisher Scientific.

2.2 | Protein Expression and Purification

To align with the experimental design, the histidine tag (His-tag) was constructed on the C-terminus of the HLA-A*02:01 heavy chain, the P14 TCR β-chain, and the 1G4 TCR β-chain, respectively. The production of both HLA-A*02:01/9 V and HLA-A*02:01/3P9V as well as the H-$2D^b$/gp33 was performed via refolding, following the same procedure previously described for H-$2D^b$/gp33 [38, 40]. The P14 TCR was produced and refolded by dilution, then purified using ion exchange and size exclusion chromatography, as previously described [38]. The 1G4 TCR was produced following previously published protocols [39].

2.3 | Fluorescent Labeling of Proteins

Proteins were fluorescently labeled using Alexa Fluor 488 or 647 NHS Ester (from here on AF488 or AF647). The fluorescent dyes were dissolved in DMSO to 5 mg/ml. The proteins were dissolved

according to the manufacturer's instructions in water or the respective buffer (Supplementary Table S1). To each 1 mL protein solution, 0.1 mL of 1 M $NaHCO_3$ (in water, pH 8.5) was added. The volume of added fluorescent dye was calculated according to Equation 1, thereby a molecular excess of 5 was used.

$$V_d = \frac{c_p \times V_p}{MW_p} \times ME \times \frac{MW_d}{c_m} \quad (1)$$

c_p – protein concentration, V_p – volume of Protein to Label, MW_p – protein Molecular Weight, ME – molar excess (number of dye molecules per protein molecule), V_d – taken Volume of the Dye Solution.

The determined fluorescent dye volume was added to the protein solution and incubated at RT for 1 h under continuous rotation. For the different pMHC and TCR molecules, the reaction was carried out at 4°C overnight to prevent aggregation or denaturation of the proteins. To purify the fluorescently labeled protein, Zeba Spin Desalting Columns with a 7 or 40 MW cutoff (ThermoFisher Scientific) were used. To prepare the columns, they were placed in a 1.5 mL tube and centrifuged at 1500 × g for 1 min to remove the storage solution. 300 µl of respective buffer was added to the top of the resin and centrifuged at 1500 × g for 1 min. This wash step was repeated twice before the protein solution was added and again centrifuged. This protein purification process was repeated once more with a fresh column. The concentration of purified protein was determined using a Nanodrop and then aliquoted and stored at −20 or −80 °C until further use.

2.4 | Surface Plasmon Resonance (SPR) Measurements

All measurements were performed on a BIAcore T200 (Cytiva) at 20 °C in a buffer containing 10 mM HEPES (pH 7.4), 150 mM NaCl, 0.005% Tween-20, 3 mM EDTA. Soluble 1G4-his_6 was noncovalently captured via an anti-His antibody immobilized on a CM5 sensor chip using standard amine coupling, using HLA-A*02:01 as the mobile phase. Approximately 5000 response units (RU) of anti-His antibody were immobilized, enabling capture of ∼1000 RU of 1G4-his_6 (TCR) (1 µM). A reference surface was prepared in parallel without 1G4-his_6. Freshly prepared HLA-A*02:01/peptide complexes (up to 100 µM) were injected over both surfaces at a flow rate of 30 µL/min, using a series of at least ten twofold dilutions, with three concentrations repeated in duplicate. The sample rack was maintained at 4 °C throughout the run. Chip surfaces were regenerated with 0.1 M Glycine-HCl (pH 2.5), 500 mM NaCl, and 0.05% Tween-20 at 30 µL/min. Specific binding signals were obtained by subtracting the response from the reference surface to eliminate bulk refractive index effects and non-specific interactions. SPR data was analyzed with BIA evaluation 3.0 software (Cytiva), K_D values were obtained from steady-state fitting of equilibrium binding curves from at least ten sample injections.

2.5 | GUV Preparation

GUVs were prepared according to a previously described protocol [41]. GUVs of the following lipid compositions were prepared: POPC:Ni-NTA (98:2 mol%) without fluorescent lipid, with 0.1 mol% ASR-PE and with 0.01 mol% TF-PE. The lipid mixture dissolved in chloroform (6 µl of 1 mg/ml) was homogenously distributed on two platinum electrodes in a custom-built Teflon chamber, dried under nitrogen stream, placed in 300 mM sucrose solution (370 µl) and GUVs were generated by electroformation at 2 V and 10 Hz for 1 h, followed by 2 V and 2 Hz for 30 min [42].

2.6 | Cell Culture Maintenance

J8 Jurkat T cells, J8 Jurkat T cells expressing ZAP70mNG, P14 Jurkat T cells and CEM cells expressing CD43 with an intracellular SNAP- and extracellular Halo-tag (CEM $CD43_{SNAP/Halo}$ kindly provided by the Sattentau lab [43]) were cultured in fully supplemented RPMI with 10% FBS at 37 °C and 5% CO_2. The cells were split regularly according to their density. Primary human T cells were isolated from peripheral blood mononuclear cells (PBMCs). PBMCs were obtained from buffy coats of healthy human donors (ethical approval by the Ethics Review Authority in Stockholm; Dnr 2025-01255-01) using density gradient centrifugation. In short, blood was diluted 1:1 with PBS and layered onto Ficoll and centrifuged at 400 xg RT for 30 min (brake off). The PBMC fraction was collected and washed with PBS three times. From PBMCs human $CD8^+$ T cells were isolated using the EasySep Human Naïve $CD8^+$ T Cell Isolation Kit II (Stemcell technologies) according to manufacturer's instructions. The isolated cells were resuspended in fully supplemented RPMI media (10% FBS, 2 mM L-glutamine, 1 mM sodium pyruvate, 1x non-essential amino acids and 10 mM HEPES) with 50 ng/mL IL-2 and subsequently activated using Human T-Activator CD3/CD28 Dynabeads (ThermoFisherScientific). The beads were removed via magnetic separation after 48 h of activation. T cells were further expanded while refreshing their media with new IL-2 every 48–72 h. To avoid T cell exhaustion, the T cells were not used longer than 14 days after activation.

2.7 | Flow Cytometry

Jurkat T cells were washed twice with PBS and stained with a viability stain (BV510 from BD Bioscience) at 1:1000 in PBS for 10 min at RT, followed by washing in staining buffer (PBS with 2% FBS). Cells were then stained with antibodies against the surface proteins CD28 (CD28-APC-H7, clone CD28.2, BD Biosciences), CTLA-4 (CTLA-4-BV421, clone BNI3, BD Horizon) and PD-1 (PD1-PE-Cy7, clone EH12.1, BD Pharmigen) 1:50 in staining buffer for 10 min at RT. For the CD45 density estimation, live Jurkat T cells were stained with ASR-PE and an antibody against CD45 (CD45-BV510, clone HI30, BioLegend). GUVs were created encapsulating 1 µM AF488, unlabeled CD45 was added (1× concentration). They were stained with ASR-PE and the CD45-BV510 antibody (more detailed description in Supplement Information). After washing the cells in staining buffer (GUVs were not washed due to their instability), flow cytometry data were acquired using a FACS Canto II system (BD Biosciences). CompBeads (BD Biosciences) were used to perform compensation for the full antibody panel, and an unstained sample was included as a control. Data analysis was performed using FlowJo 10.7.1 (FlowJo LLC).

2.8 | Cell Preparation for Imaging

Generally, for immune synapse reconstitution experiments, the cells were prepared immediately prior to imaging. Cells were washed twice with the respective buffer of the protein (800 ×g for 1 min) and resuspended in 500 µl of buffer. For additional lectin-staining, cells were incubated with 1 µg/ml WGA-AF647 or AAL-647, or 10 µg/ml SNA-AF647 or MAL-II-AF647 at RT for 20 min, washed twice with the respective buffer (800 ×g for 1 min) and resuspended in 500 µl buffer. For Ca^{2+} imaging, the cells were washed twice with L-15 medium (500 ×g for 3 min) and resuspended in 100 µl L-15 medium. Fluo-4, AM (1 µl) was added and incubated at 37°C for 15 min before washing the cells thrice with PBS. For staining of the CEM $CD43_{SNAP/Halo}$ cells, the SiR-tagged SNAP-substrate or Halo-ligand (500 nM final concentration) was added to the cells. After incubation for 30 min (SNAP-substrate) or 1 h (Halo-ligand), the cells were washed twice in PBS.

2.9 | GUV Labeling

For immune synapse reconstitution experiments, GUVs were decorated with different fluorescently labeled or unlabeled proteins (see Supplementary Table S1 for a complete list of proteins and their fluorescent label). To a tube containing 100µl buffer, 100 µl GUV solution was added. Depending on the experiment, different amounts of protein(s) were added as indicated in Supplementary Table S2. In short, a total protein amount of approximately 2.5 or 1.25 pmol was added to GUVs for artificial or semi-artificial reconstitutions, respectively. This ensured better contrast in the imaging of semi-artificial contacts. For protein exclusion titration experiments, the amount of binding protein was held constant, while the amount of excluded protein was varied. GUVs were incubated with the proteins at RT for 30 min, protected from light on a rotator set to low speed (8–10 rpm). GUVs were not washed prior to imaging. For the no-protein control, cells and GUVs were stained with 100 nM NR12A.

2.10 | Fluorescent Confocal Imaging and Lattice Light-Sheet Microscopy

The reconstituted immune synapses were imaged in previously blocked (3 mg/ml BSA in PBS) µ-Slides (18-well glass bottom, ibidi). To assess the contacts, 80 µl of respective buffer and 40 µl of each GUV population (artificial contacts); or 40 µl GUVs and 40 µl washed cells (semi-artificial contacts) were added into the well. In confocal imaging, artificial contacts and semi-artificial contacts with Jurkat T cells were imaged at RT, whereas semi-artificial contacts with activated human primary $CD8^+$ T cells were imaged at 37°C. A Zeiss LSM980 confocal microscope with a Zeiss water immersion objective, C-Apochromat 40X/1.2 NA, was utilized. 488 nm or 639 nm lasers were used to excite the AF-488 or AF-647 conjugated proteins, ZAP70mNG or fluorescent lipid dyes. We performed fast volumetric imaging with lattice light sheet microscopy (LLSM) using the Zeiss Lattice Lightsheet 7. ZAP70mNG and Fluo- 4 or AF-647 conjugated proteins were excited with 488 nm or 640 nm lasers, respectively. In lattice light-sheet imaging, semi-artificial contacts with Jurkat T cells were imaged at 37°C. Time-lapse imaging of cell-GUV contacts was performed with time intervals of 5 seconds.

2.11 | Image Analysis

Confocal images and their protein signal intensities were analyzed using Fiji (for a detailed description of the analysis, refer to the Supplementary Information) [44]. In short, the regions of contact and outside the contact were defined by intensity thresholding in the respective channels and manual selection. The intensity outside the contact was normalized to 1; at artificial contacts, the outside signal is the sum of the intensities of each individual GUV. The intensity at the contact was then normalized to the outside. Values higher than 1 indicate enrichment of protein at the contact, whereas values lower than 1 indicate exclusion of the protein from the contact. To generate intensity profiles along the GUVs, the VISION software [45] employing single object detection was utilized with signal intensities normalized to the maximum signal in the profile. LLSM data were deskewed using the Zeiss software ZEN 3.11, and videos were prepared using Imaris 10.2.0.

3 | Results and Discussion

We utilized model membranes to reconstitute cell–cell contacts bottom-up with controllable lipid and protein compositions. Here, we used GUVs containing 2 mol% Ni-NTA functionalized lipids to attach His-tagged proteins to their surface (Figure 1A) [6, 31]. By fluorescent labeling of the proteins of interest, contact formation was examined in confocal fluorescent imaging. In the next sections, we will mainly focus on proteins involved in the formation of the T cell immune synapse.

3.1 | Artificial Model System (GUV–GUV)

3.1.1 | Adhesion Proteins, TCR-pMHC and Checkpoint Proteins Enrich at the Contact Site

To test our artificial model system, we examined contact formation of GUVs decorated with either CD2 or CD58, adhesion proteins typically found on lymphocytes and known to bind one another [4, 46]. We quantified the enrichment and exclusion of proteins at the interface (Supplementary Figure S1). The enrichment factor is the intensity fold change at the interface compared to the non-interface part (from here on called “outside”). We thereby normalized to the sum of intensities outside the contact to account for the presence of two membranes at the contact. Values higher than 1 indicate enrichment of protein at the contact, whereas values lower than 1 indicate exclusion of the protein from the contact. CD2- and CD58-GUVs formed a contact at which both CD2 and CD58 were clearly enriched compared to the outside (Figure 1B). This enrichment was also observed in the linearized profiles of the respective GUVs (Figure 1B, right panel). In contrast, neither CD58 nor CD2 alone bound to themselves or were enriched at the contact (Supplementary Figure S2). We thereby confirmed that our artificial contact formation is specific to the presence of two binders on two opposite sides. We did not observe synapse formation due to unspecific binding, and

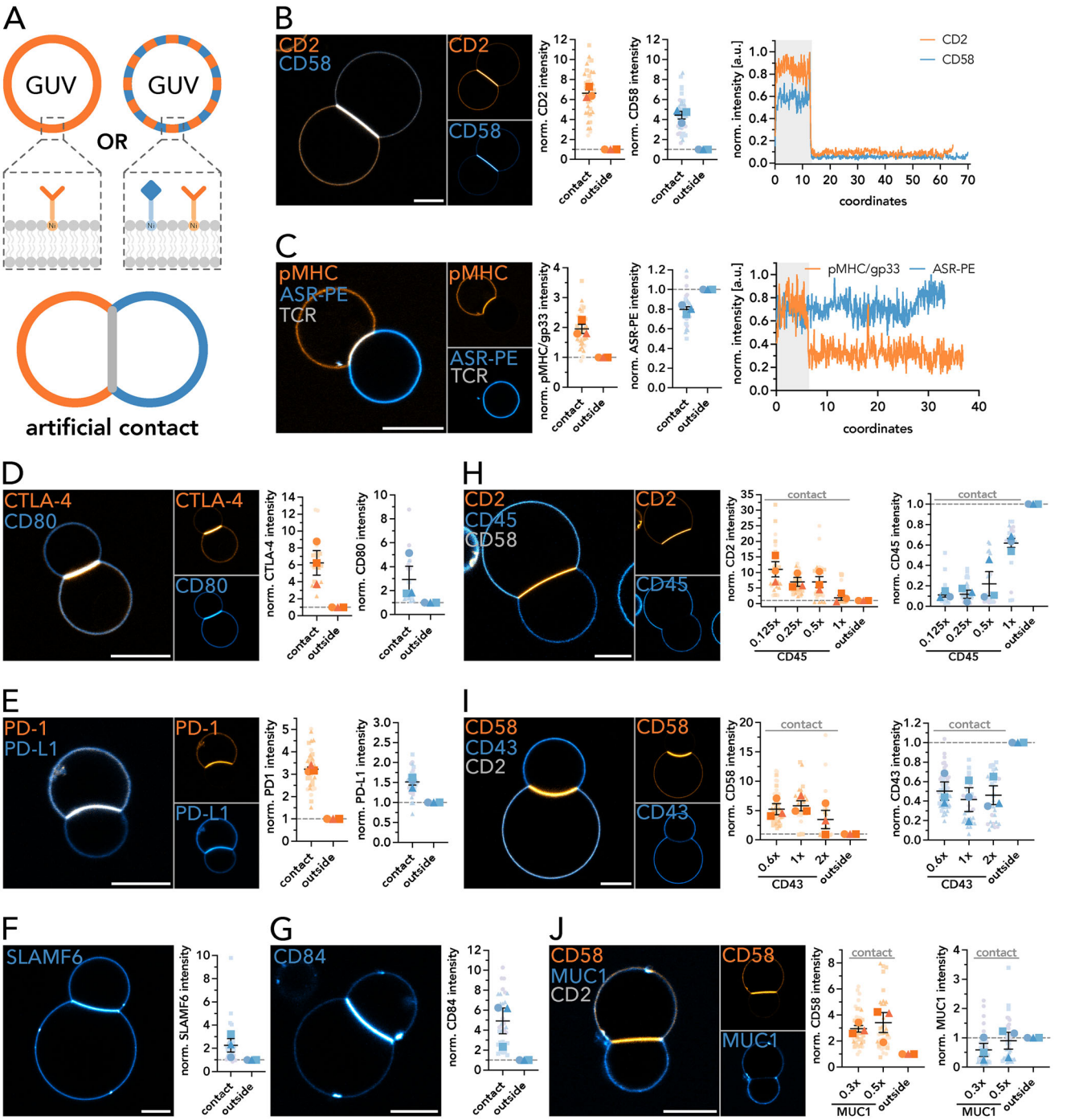

FIGURE 1 | Artificial immune synapse reconstitution using free-standing GUVs. A) Schematic representation of the artificial immune synapse reconstitution using GUVs. His-tagged fluorescently labeled proteins are attached to the GUV membranes via Ni-lipids. B) Representative confocal image of CD2-CD58 contact formation (left). CD2-AF488 and CD58-AF647 intensity at the contact and outside was quantified and normalized (middle). Linearized fluorescence intensity profiles of the GUVs in the confocal image with the contact highlighted in grey (right). C) Representative confocal image of pMHC/gp33-P14 TCR contact formation (left). P14 TCR has no fluorescent label and was reconstituted on GUVs incorporating Abberior Star Red labeled PE lipid (ASR-PE). pMHC/gp33-AF488 and ASR-PE intensity at the contact and outside was quantified and normalized (middle). Linearized fluorescence intensity profiles of the GUVs in the confocal image with the contact highlighted in grey (right). D-E) Representative confocal images of CTLA-4-CD80 (D) and PD-1-PD-L1 (E) contact formation (left). CTLA-4-AF488, CD80-AF647, PD-1-AF488 and PD-L1-AF647 intensity at the contact and outside was quantified and normalized (right). F-G) Representative confocal images of SLAMF6 (F) and CD84 (G) contact formation (left). SLAMF6-AF647 and CD84-AF647 intensity at the contact and outside was quantified and normalized (right). H-J) Representative confocal images of 0.125x CD45 (H), 0.6x CD43 (I) and 0.3x MUC1 (J) exclusion at the CD2-CD58 contact. Intensities of CD2-AF488 or CD58-AF647 combined with increasing amounts of CD45-AF647, CD43-AF488 or MUC1-AF488 at the contact and outside were quantified and normalized (right). Superplots show individual contacts as small symbols. Large symbols depict the mean of the individual biological replicates. Symbol corresponds to the individual biological replicate ($n \geq 3$). Standard error of the mean is shown. Scale bar corresponds to 10 μm.

lipids that are freely diffusing in the bilayer did not get enriched or depleted (Supplementary Figure S2). Besides the adhesion receptor pair CD2:CD58, we also examined contact formation of GUVs decorated with the main ligand receptor-pair involved in T cell signaling: pMHC and TCR. Here, we used the MHC class I H-2D^b presenting the gp33 peptide (KAVYNFATM) derived from lymphocytic choriomeningitis virus (LCMV) (from here on referred to as pMHC/gp33) and the P14 TCR, which bind each other with an affinity of 3±0.5 μM and fast kinetics with k_{off} = 1 s^{-1} [47]. The P14 TCR could not be fluorescently labeled due to stability issues. GUVs reconstituted with pMHC/gp33 clearly formed contacts with P14 TCR-GUVs stained with a lipid dye, at which pMHC/gp33 was enriched (Figure 1C). Interestingly, the pMHC/gp33 also formed a self-binding interface (Supplementary Figure S2).

Being the target of cancer immunotherapies, CTLA-4 and PD-1 are checkpoint inhibitor proteins expressed on the T cell surface. Binding to their ligands, such as CD80 and CD86 or PD-L1 and PD-L2, respectively, attenuates and regulates downstream T cell signaling [48, 49]. GUVs decorated with CTLA-4 and CD80 formed a contact at which both proteins enriched (Figure 1D), which was not observed in the single protein controls (Supplementary Figure S2). Similarly, PD-1 and PD-L1 triggered GUV–GUV contact formation with enrichment of the proteins at the contact (Figure 1E and Supplementary Figure S2). PD1 alone did not form a real contact, whereas PD-L1 alone triggered contact formation at which PD-L1 also enriched (Supplementary Figure S2).

Inspired by this homotypic contact formation, we also tested other proteins that are reported to interact homotypically. As members of the signaling lymphocyte activation molecule (SLAM) family, SLAMF6 and CD84 share high structural similarity, are expressed by different lymphocytes, and form *trans*-homophilic interactions [50, 51]. Both co-stimulatory and co-inhibitory functions have been reported for SLAMF6 [52–54] and CD84 [50, 55]. Reconstituted on GUVs, both SLAMF6 and CD84 triggered contact formation and enriched at the contact (Figure 1F,G and Supplementary Figure S2).

It is important to note that with the enrichment of the proteins at the contact site, there may be extensive protein crowding and an increased risk for protein aggregation at the contact, especially in the artificial model system as there is no active process controlling the distribution of surface proteins as would be the case at a regular cell–cell contact. Additionally, we have observed various geometries of the GUV–GUV interfaces with straight, slightly curved or fully curved contacts. The reasons for these differently shaped interfaces are multi-factorial and are likely influenced by the individual bending rigidities of the GUV membranes, their tension, and apparent densities as well as binding affinities of the proteins reconstituted on the GUV surface [56].

3.1.2 | Heavily Glycosylated Proteins CD45, CD43, and MUC1 Are Excluded From the Contact

At cell–cell interfaces, including immune cell contacts, numerous proteins locally enrich, whereas others get segregated or excluded locally. Segregation of CD45 has been reported from both the central and peripheral SMACs of the immune synapse [4, 15], from TCR microclusters [57], at submicron-scale close contacts [58] as well as the tips of T cell microvilli [59]. Therefore, we examined CD45 distribution in our artificial model system. In addition to CD2 and CD58 forming a stable contact, we added increasing amounts of CD45 to both GUV species and examined contact formation (Figure 1H). CD45 was typically excluded from the CD2-CD58 contact, as clearly observable in linearized GUV profiles in Supplementary Figure S2. As our artificial model system only allows passive protein distribution, driven by diffusion or mediated by protein–protein interactions, rather than by cytoskeletal or active transport mechanisms, our results suggest that the exclusion of CD45 is due to a physical mechanism, such as size-dependent segregation. The distance that CD2-CD58 proteins span at the cell–cell interface (~130 Å) is shorter than the extracellular domain (ECD) of CD45 (even for its smallest isoform), which is rigid and usually oriented upright, leading to passive segregation of CD45 [58, 60]. The ECD of CD45 is also heavily glycosylated, adding to the bulkiness of the protein [61]. We observed that increasing amounts of CD45 hindered contact formation and decreased CD2 enrichment and CD45 exclusion at the contact (Figure 1H and Supplementary Figure S4). At the highest protein concentration, contact formation was often completely prevented (Supplementary Figure S4). Given the constant amounts of CD2 and CD58 molecules and the smaller size of the CD2-CD58 complex compared to the CD45 ECD size, the interactions between CD2 and CD58 appear to be insufficient to form a contact and exclude CD45 from the contact site, when CD45 is present in higher densities.

To estimate whether the CD45 density on the GUVs is within the physiological range, we have performed flow cytometry analysis to compare the CD45 density on the GUVs with those on Jurkat T cells (Supplementary Figure S5; for a detailed description of the CD45 density estimation see Supplement Information). In short, we confirmed that GUVs of certain sizes remained intact during flow cytometry, determined their size and normalized the CD45 intensity to their surface area. We observed that the CD45 density on GUVs (0.5x condition) was about double compared to Jurkat T cells. Therefore, the reconstituted amounts cover the physiological range of CD45 expression (corresponds to 0.25x condition) and at densities higher than the physiological level, exclusion of CD45 becomes less efficient.

We also examined the distribution and influence on contact formation of the heavily glycosylated proteins CD43 and MUC1, which are highly expressed on lymphocytes and serve as a physical barrier [62–65]. Similar to CD45, CD43 and MUC1 were excluded from the CD2-CD58 mediated contact and increasing glycoprotein amounts led to reduced CD58 enrichment as well as less glycoprotein exclusion (Figure 1I,J and Supplementary Figure S2). As described above, due to the large size and bulkiness of their ECDs, CD43, and MUC1 were passively segregated from the CD2-CD58 mediated contact. High concentrations of CD43 also prevented contact formation, even when the GUVs were in close proximity (Supplementary Figure S4). At the T cell immune synapse, CD43 is excluded, but according to previous studies in an active process. For example, some ezrin-radixin-moesin (ERM) family proteins link cell surface proteins to the actin cytoskeleton by interacting with the cytoplasmic tails of CD43 [66, 67]. After TCR signaling activation, CD43 is actively moved away from the

immune synapse [68, 69]. Thus, CD43 exclusion from the IS seems to be both a passive process driven by kinetic segregation and an active process mediated by ERM proteins. MUC1 has also been proposed to function as a co-inhibitory molecule in T cell signaling [70]. At high concentrations, MUC1 was also found to be enriched at parts of the GUV–GUV contact, which is counter-intuitive given its large size and extensive glycosylation. The enrichment could be due to protein–protein interactions, as MUC1 self-aggregation via a self-aggregation domain in the ECD was previously suggested [71]. Also carbohydrate-carbohydrate interactions are likely a cause for MUC1 enrichment at high density, as they were reported to be implicated in mucin self-aggregation as well as cellular interactions in general [72, 73]. Nonetheless, MUC1 was locally excluded from regions of CD58 enrichment (Supplementary Figure S4), indicating that at sites of CD2-CD58 binding, the opposing GUV membranes are in too close proximity for MUC1 to occupy the interface. Among the highly glycosylated proteins, MUC1 was the only one showing this behavior at high concentrations, a phenomenon that requires further investigation.

3.1.3 | The Artificial Model System Can be Used for Non-T Cell Interfaces

The artificial model system is also applicable to other immune cell contacts. To show this versatility, we selected two examples: (i) the tumor antigen B7-H6, which binds the NKp30 receptor on NK cells, triggering their activation [74]; and (ii) the "Don't-eat-me" ligand CD47, expressed on all cells in the body and its inhibitory receptor SIRPα preventing uptake by phagocytes [75, 76]. B7-H6 and NKp30 (unlabeled due to instability) formed a contact at which B7-H6 was enriched, whereas in the B7-H6 only control, no protein enrichment was observed (Supplementary Figure S3). GUVs decorated with CD47 formed contacts with GUVs presenting SIRPα on their surface, resulting in CD47 enrichment at the interface, whereas SIRPα was only slightly enriched (Supplementary Figure S3). In the individual protein controls, no clear contact formation was observed (Supplementary Figure S3).

3.2 | Semi-Artificial Model System (Cell-GUV)

3.2.1 | Adhesion Molecules Mediate Contact Formation

Next, we wanted to explore whether these protein reorganizations can be seen in semi-artificial model systems where a cell is combined with a GUV. We focused on T cells and investigated contact formation with both Jurkat T cells and activated human primary $CD8^+$ T cells (hereafter referred to as $CD8^+$ T cells). We reconstituted proteins on the GUVs and added T cells to assess contact formation and protein distribution (Figure 2A). Thereby, a contact was determined by enrichment of the protein or by shape deformation of the GUV at the potential contact site with the cell. We started with the adhesion receptor pair CD2-CD58. Jurkat T cells formed contacts with GUVs decorated with either CD2 or CD58, and both proteins enriched at the interface, with CD2 showing stronger enrichment (Figure 2B,C, Supplementary Figure S6). This indicates that although both proteins are expressed on Jurkat T cells, CD58 is expressed at higher levels. $CD8^+$ T cells also formed contacts with CD58-decorated GUVs, where CD58 was enriched at the interface. In contrast, binding to CD2 only rarely led to contact formation and enrichment of CD2 at the contact (Figure 2D,E and Supplementary Figure S8). While CD58 is expressed by a broad range of both human hematopoietic and nonhematopoietic cells, including T cells, expression of CD2 is restricted mainly to T and NK cells. CD2 is the main adhesion receptor for $CD8^+$ T cells, binding to its ligand CD58 on target cells or antigen-presenting cells (APCs) [77], explaining our enrichment results. To ensure that binding was specific to the proteins reconstituted on the GUVs, we tested for the binding of Jurkat T cells and $CD8^+$ T cells to protein-free GUVs and found that while cells were often in close proximity to the GUVs, no real contact was formed (Supplementary Figures S6 and S8). Additionally, blocking CD2 on the GUVs using a monoclonal anti-CD2 antibody prevented contact formation between Jurkat T cells and GUVs (Supplementary Figure S6). This confirmed that T cell binding to the GUVs was indeed mediated by CD2-CD58 binding.

3.2.2 | Bulky Glycoproteins Are Effectively Segregated From the Contact

Similar to the artificial contacts, we also examined the distribution of glycoproteins CD45, CD43 and MUC1 at the CD2-CD58 mediated contact in the semi-artificial model system. For $CD8^+$ T cells, we reconstituted CD58 on the GUV to trigger contact formation, whereas for Jurkat T cells we reconstituted CD2, as it enriched more at the GUV-Jurkat T cell contact. For both Jurkat T cells and $CD8^+$ T cells, we observed exclusion of CD45, CD43 and MUC1 at the CD2-CD58 mediated contact (Figure 2F–K). The CD45 exclusion at T cell contacts is consistent with previous findings and has also been observed for B cell [78], macrophage [79], basophil and mast cell contacts [80]. With increasing amounts of CD45, CD43 or MUC1 added, we discovered a decrease in CD2 enrichment and glycoprotein exclusion at the Jurkat-T cell – GUV contact (Figure 2F–H). Interestingly, this effect was most pronounced for CD45. The determined physiological range of CD45 density on Jurkat cells is covered by the reconstituted CD45 on the GUVs (corresponds to 0.5x condition). Similar to the artificial model system, at reconstituted densities higher than the physiological level, exclusion of CD45 becomes less efficient (Supplementary Figure S5). The enrichment of CD2 relative to the exclusion of glycoproteins was particularly evident in linearized example profiles (Supplementary Figure S6). A clear CD58 enrichment relative to the exclusion of CD45, CD43 and MUC1 was also visible at the $CD8^+$ T cell – GUV contact (Figure 2I–K and Supplementary Figure S8). Compared to the fully artificial model system, the membrane distance of the cell-GUV contact is not solely defined by the CD2-CD58 complex size, and the interface is likely more heterogeneous since cell surfaces harbor many additional proteins beyond CD2 or CD58. Nonetheless, the inter-membrane distance seems small enough to enable effective size-dependent segregation of the ECDs of CD45, CD43 and MUC1. So far, we have shown the protein distribution on the GUV surface. To address whether the proteins are reorganized on the live cell surface, we examined the distribution of CD43 on the cell surface upon contact formation with GUVs (Supplementary Figure S7). For this, we utilized CEM cells expressing CD43 with an endogenous intracellular SNAP-tag as well as extracellular Halo-tag [43]. Upon contact formation of these cells with CD2 reconstituted on GUVs, CD43 is excluded

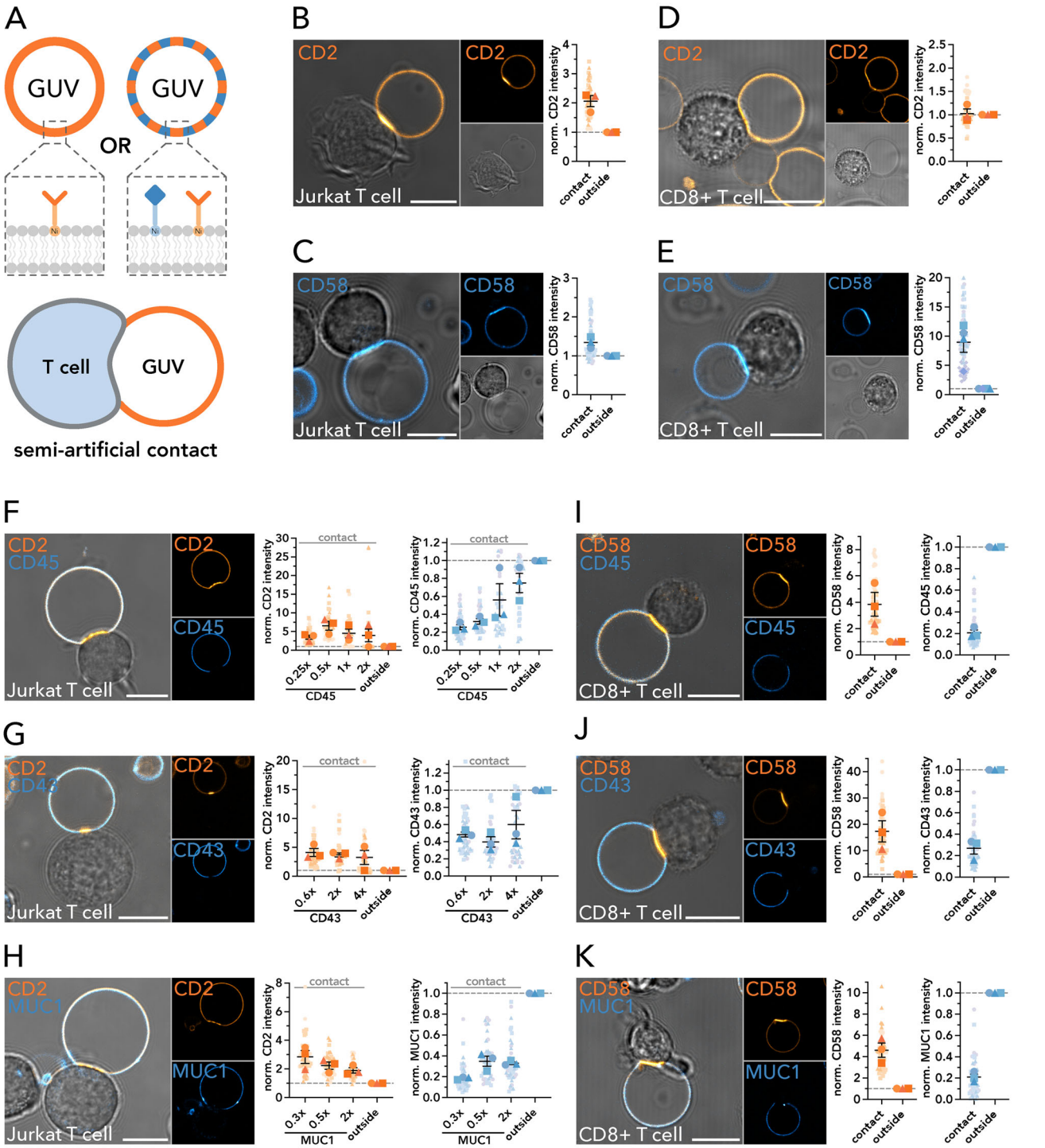

FIGURE 2 | Semi-artificial immune synapse reconstitution using free-standing GUVs with Jurkat and human primary T cells. A) Schematic representation of the semi-artificial immune synapse reconstitution using GUVs in combination with Jurkat J8 T cells or activated human primary CD8+ T cells. His-tagged fluorescently labeled proteins are attached to the GUV membranes via Ni-lipids. B,C) Representative confocal images of contact formation between GUVs decorated with CD2 (B) or CD58 (C) with Jurkat T cells (left). CD2-AF488 and CD58-AF647 intensity at the contact and outside was quantified and normalized (right). D-E) Representative confocal images of contact formation between GUVs decorated with CD2 (D) or CD58 (E) with activated human primary CD8+ T cells (left). CD2-AF488 and CD58-AF647 intensity at the contact and outside was quantified and normalized (right). F-H) Representative confocal images of contact formation between GUVs decorated with CD2 and 0.25× CD45 (F), 0.6× CD43 (G) or 0.3× MUC1 (H) with Jurkat T cells (left). Intensities of CD2-AF488 or CD58-AF647 combined with increasing amounts of CD45-AF647, CD43-AF488 or MUC1-AF488 at the contact and outside were quantified and normalized (right). I-K) Representative confocal images of contact formation between GUVs decorated with CD58 and CD45 (I), CD43 (J) or MUC1 (K) with activated human primary CD8+ T cells (left). CD58-AF488 and CD45-AF647; CD58-AF647 and CD43-AF488; or CD58-AF647 and MUC1-AF488 intensity at the contact and outside was quantified and normalized (right). Superplots show individual contacts as small symbols. Large symbols depict the mean of the individual biological replicates. Symbol corresponds to the individual biological replicate (n = 3). Standard error of the mean is shown. Scale bar corresponds to 10 μm.

at the cell surface, confirming the protein reorganization at the cell surface. Additionally, to test whether smaller contacts might occur, for example, via microvilli interactions causing protein redistribution, we used large unilamellar vesicles (LUVs, 50–100 nm) instead of GUVs. The CD43 exclusion on the cell surface was notable but much less pronounced for LUV contact sites given their small size (around 200 nm) and the confocal microscopy resolution limit (Supplementary Figure S7). Together, the results demonstrate that the CD43 exclusion observed on the GUV surface also occurs at the cell surface and this likely holds true for CD45 and MUC1.

Similar to the GUV–GUV contacts, at high glycoprotein concentrations, contact formation between Jurkat T cells and GUVs was frequently prevented, even when both were in close proximity (Supplementary Figure S9). CD43 and MUC1, among other glycoproteins, serve as a physical barrier on the cell surface and have been shown to interfere with T cell adhesion. CD43 and MUC1 are actively pushed out of the immune synapse [68, 69]; or act as coinhibitory molecules in T cell signaling, respectively [62, 70]. Interestingly, their presence not only affects the T cell synapse, but also the phagocytic or NK cell synapse. CD43 and MUC1 are shed from the cell surface during apoptosis, thereby enhancing the uptake by phagocytic cells [43]. In cancer, MUC1 shields adhesion and death receptors, preventing immune cell binding [65, 81] and, together with CD43, increases target cell resistance to NK cell-mediated lysis [82]. As we also observed this shielding behavior, our model systems could provide a tractable platform to study how heavily glycosylated proteins such as CD43 and MUC1 modulate or prevent specific interactions at the cell–cell interface.

3.2.3 | Immune Checkpoint Proteins Do Not Enrich at the Contact

Further, we examined contact formation between T cells and GUVs reconstituted with immune checkpoint proteins. We chose to present CD80 on the GUV as a ligand for CTLA-4 (co-inhibitory) or CD28 (co-stimulatory) receptors expressed on T cells [83], and PD-L1 as a ligand for the co-inhibitory receptor PD1 [49]. These receptor-ligand pairs are recruited to the immune synapse [4]. GUVs decorated with CD80 or PD-L1 were slightly deformed upon interaction with Jurkat or $CD8^+$ T cells, indicating bona fide contact formation. However, no consistent enrichment of the checkpoint proteins was observed at the contact site (Supplementary Figures S6 and S8). The Jurkat T cell clone used in this study lacks CTLA-4 and expresses only very low levels of PD1 and moderate levels of CD28, and therefore serves as a control (Supplementary Figure S6). As expected, we observed little to no PD-L1 enrichment at the Jurkat-GUV contact site, due to the low PD1 expression level. In contrast, the absence of CD80 enrichment was surprising as Jurkat cells express CD28. Also, the lack of enrichment of CD80 and PD-L1 at the contact with $CD8^+$ T cells was unexpected, as previous studies reported upregulation of CTLA-4 and PD1 upon activation with anti-CD3/CD28 Dynabeads [84], along with sustained expression of CD28 [85]. The reason for the missing enrichment is most likely due to the nature of the binding of these ligand-receptor pairs. Reconstitution of CD80 and PD-L1 alone may be insufficient to form a stable contact, requiring additional TCR-pMHC engagement or adhesion molecule binding. In fact, a previous study reported that proper CD28-CD80 engagement required prior adhesion mediated by CD2 [86]. Further, in the absence of TCR engagement, CD28 binding to CD80 does not cause T cell activation, as it binds CD80 only monovalently and with low affinity. Upon TCR engagement, however, CD28 undergoes a conformational change that enables bivalent binding to CD80, thereby strengthening the interaction [87]. As there is no additional TCR engagement or adhesion molecule binding at our cell-GUV contacts, CD28-CD80 or PD1-PD-L1 interactions are likely too weak to sustain stable binding, and therefore, no CD80 or PD-L1 enrichment on the GUVs is observed. Additionally, the upregulation of CTLA-4 or PD-1 is dynamic; hence, it is possible that their expression at the time point of imaging was too low to permit detectable enrichment of the corresponding ligands presented on the GUV at the contact site.

3.2.4 | Homophilic Binding Proteins Rarely Enrich at the Contact

Reconstitution of the homophilic proteins SLAMF6 and CD84 on GUVs triggered contact formation with Jurkat and $CD8^+$ T cells; however, enrichment of these proteins at the contact was only rarely observed (Supplementary Figures S6 and S8). As SLAMF6 and CD84 are expressed on activated $CD8^+$ T cells [50, 88–90] as well as on Jurkat T cells [90, 91], it is surprising that enrichment at the contact was only occasionally observed. The SLAM family proteins belong to the CD2 superfamily immunoglobulin (Ig) domain-containing molecules. Consequently, the homophilic interactions of CD84 and SLAMF6 share several structural and functional similarities to the CD2-CD58 interaction [50, 92]. The distance spanned by a CD84 *trans*-dimer (~140 Å) falls within the range of the CD2-CD58 and TCR-pMHC interactions [50]. It is therefore unlikely that additional adhesion molecules or TCR-pMHC engagement are required for proper contact formation and for CD84 or SLAMF6 enrichment. Nonetheless, the SLAMF6 or CD84 levels on the cell side may have been too low to permit detectable enrichment of the corresponding proteins presented on the GUV at the contact site.

3.2.5 | Semi-Artificial Model System Can Distinguish Peptides of Different Affinity

As the main ligand-receptor pair in T cell signaling, crucial for triggering downstream protein interactions and subsequent T cell activation, we examined the TCR-pMHC interaction in the semi-artificial model system. We decorated the GUVs either with the pMHC/gp33 alone (as described above) or in combination with CD45 and added Jurkat T cells that express the P14 TCR (Figure 3A and Supplementary Figure S10). We observed contact formation accompanied by enrichment of pMHC/gp33 at the contact site and exclusion of CD45, confirming previous literature [93]. The enrichment of pMHC/gp33 was typically discontinuous, appearing as localized puncta rather than uniform accumulation along the entire contact interface. In areas with low pMHC/gp33 enrichment, CD45 was not fully excluded, a pattern that becomes especially apparent in the linearized GUV profile (Supplementary Figure S10). This suggests a more heterogeneous membrane topology, with variable distances between the cell and GUV

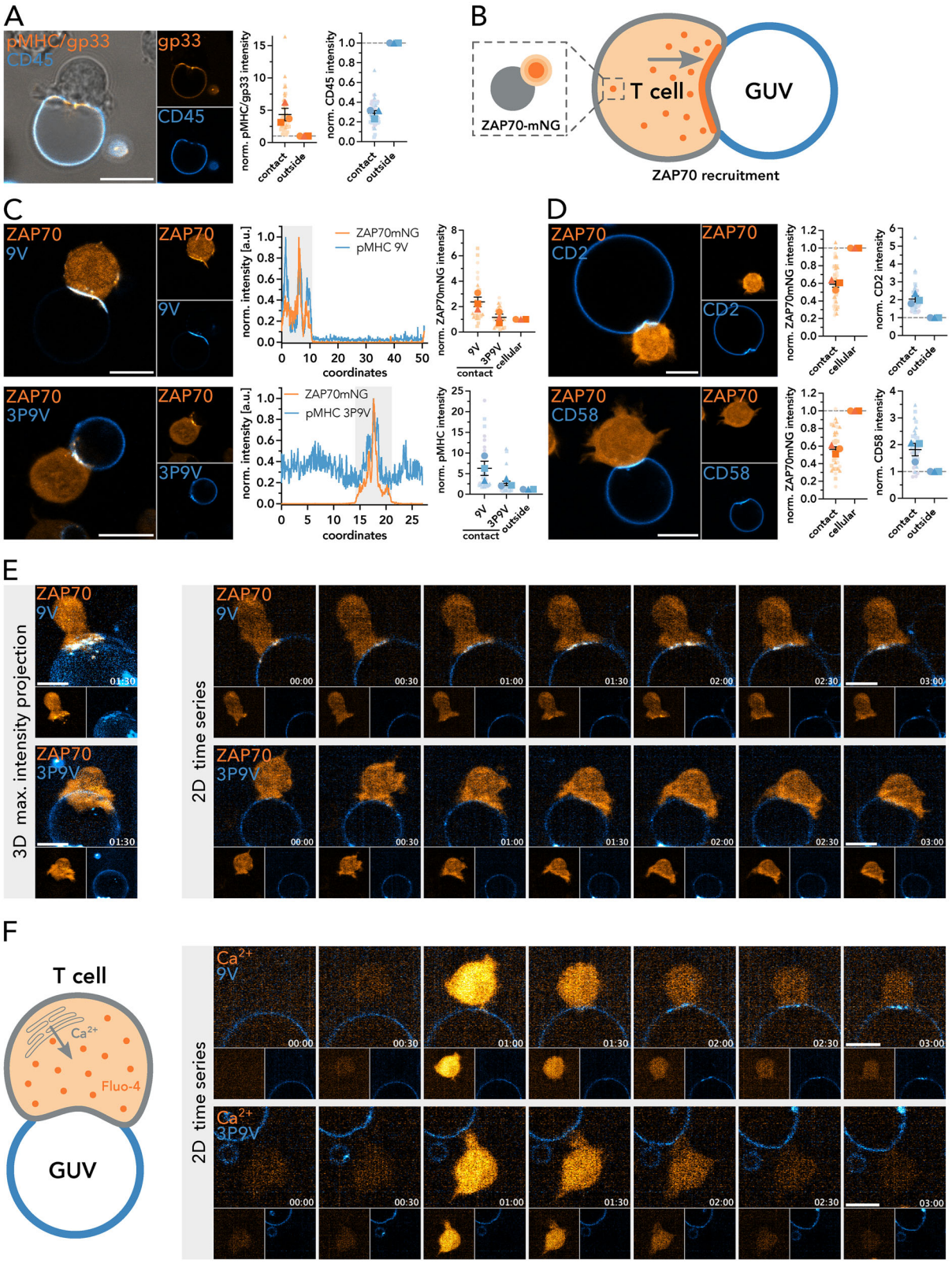

FIGURE 3 | T cells get activated at TCR-pMHC mediated T cell-GUV contact. A) Representative confocal images of contact formation between GUVs decorated with pMHC/gp33 and CD45, and Jurkat P14 T cells (left). pMHC/gp33-AF488 and CD45-AF647 intensity at the contact and outside was quantified and normalized (right). B) Schematic representation of the ZAP70mNG Jurkat T cell line and ZAP70 recruitment to the T cell-GUV contact. C) Representative confocal images of contact formation between GUVs decorated with pMHC/9 V or pMHC/3P9V and ZAP70mNG expressing Jurkat T cells (left). Linearized fluorescence intensity profiles of the GUVs in the confocal images with the contact highlighted in grey (middle). pMHC/9V-AF647 or pMHC/3P9V-AF647 and ZAP70mNG intensities at the contact and outside or within the cell were quantified and normalized (right). D) Representative confocal images of contact formation between GUVs decorated with CD2 or CD58 and ZAP70mNG expressing Jurkat T cells (left). CD2-

membranes. The distance spanned by TCR-pMHC interaction (~150 Å) is smaller than the ECD of CD45, causing its spatial segregation [58]. According to the kinetic segregation model [94], this exclusion creates a low-phosphatase environment that permits TCR phosphorylation and signaling. The size disparity is critical, as the small size of TCR-pMHC pairs promotes signaling [95], whereas ECD-truncation of CD45 inhibits it [96]. The puncta structures of pMHC/gp33 on the GUV are in accordance with the formation of TCR-pMHC microclusters during the initial stages of immune synapse formation [97, 98]. Following TCR microcluster formation, the Src family kinase Lck phosphorylates the Immunoreceptor Tyrosine-based Activation Motifs (ITAMs) of the TCR, resulting in recruitment and activation of the kinase ZAP70. Activated ZAP70 then phosphorylates membrane-associated adaptor protein LAT (linker of activated T cells), which in turn recruits phospholipase Cγ (PLCγ) and promotes its activation. PLCγ activation triggers calcium release and downstream activation of Ras and PKC, ultimately resulting in T cell activation [4]. Therefore, recruitment of ZAP70 serves as an early indicator of T cell activation, whereas Ca^{2+} release represents a later readout. To examine ZAP70 recruitment in our semi-artificial model system, we used Jurkat T cells expressing ZAP70 tagged with the fluorescent protein mNeonGreen (ZAP70mNG). If T cell signaling is triggered by the proteins reconstituted on the GUV, ZAP70mNG should be recruited to the contact site (Figure 3B), as demonstrated in previous studies using reconstituted T cell synapses [35, 93]. We utilized the same MHC class I molecule (HLA-A*0201) presenting two different peptides: 9 V (SLLMWITQV) and 3P9V (SLPMWITQV). While the 9 V variant is efficiently recognized by the 1G4 TCR [39], the 3P9V variant is not. Examined by surface plasmon resonance (SPR), the 1G4 TCR binds to the 9 V and 3P9V variants with affinities of 5.2 and 16.6 μM, respectively (Supplementary Figure S10). We compared both enrichment at the contact and ZAP70mNG recruitment (Figure 3C). While pMHC/9 V was enriched across almost the entire contact, pMHC/3P9V showed lower enrichment, appearing more punctate and discontinuous (Figure 3C and Supplementary Figure S10). Consistent with the binding affinities, ZAP70mNG recruitment was higher at pMHC/9 V contacts compared to pMHC/3P9V. Thus, our semi-artificial system is sensitive to differences in TCR-pMHC affinities. In pMHC-only controls, both pMHC/9 V and pMHC/3P9V were enriched at the contact in the artificial system (Supplementary Figure S10). As expected, ZAP70mNG recruitment did not occur when only CD2 or CD58 were reconstituted on the GUVs (Figure 3D and Supplementary Figure S10).

These results are consistent with the role of pMHC as the primary antigenic signal in T cell activation. The CD2-CD58 interaction stabilizes contact formation and serves as a second signal in T cell activation, but does not trigger T cell signaling on its own [77, 99]. The seemingly decreased ZAP70mNG intensity reflects its intracellular localization. ZAP70mNG is therefore only partly present in the contact region defined by CD58 in the analysis (see Supplementary Figure S1). To qualitatively examine the distribution of pMHC/9 V, pMHC/3P9V, and ZAP70 in greater detail, we performed lattice light-sheet microscopy (LLSM) for fast volumetric live-cell imaging over time with minimal phototoxicity (Figure 3E) [100]. Jurkat T cells clustered pMHC/9 V on the GUVs, and a local ZAP70 enrichment was observed at these pMHC/9 V clusters. The ZAP70 enrichment closely tracked with the pMHC/9 V clusters over time (Figure 3E). In contrast, hardly any pMHC/3P9V cluster formation or ZAP70 recruitment was observed, even though the cells actively engaged with GUVs presenting pMHC/3P9V (Figure 3E an). As an additional early indicator of T cell signaling, we investigated calcium release using Fluo-4 following Jurkat T cell interaction with GUVs reconstituted with either pMHC/9 V or pMHC/3P9V (Figure 3F). While calcium flashes were observed in Jurkat T cells upon interaction with GUVs for both peptides, only the pMHC/9 V accumulated in clusters that moved toward the centre of the cell-GUV contact (Figure 3F). Performing 4D LLSM to capture the initial contact between a cell and a GUV in the semi-artificial model system is technically challenging, as both recording the first contact event and analyzing the resulting 4D data are not trivial. Future experiments should focus on quantification pMHC cluster formation, ZAP70 recruitment and calcium flashes to allow a more accurate interpretation of the results. Nonetheless, we could successfully demonstrate with limited data that live T cell contact formation and activation can be qualitatively examined in our model system using volumetric imaging.

3.2.6 | Lectin Binding Suggest Differential Sugar Residue Distribution at the Contact

Besides MUC1, CD43, and CD45, numerous other cell surface proteins, and a wide range of lipids, are glycosylated to varying extents. In humans, glycans are synthesized in the endoplasmic reticulum and Golgi apparatus through the stepwise addition of monosaccharides connected by glycosidic bonds [101]. The vast complexity of glycosylation arises from the ten different monosaccharides existing in either α- or β-anomers, the nature of the glycosidic bond, the various combinations of these monosaccharides into glycans of different chain lengths, and branching patterns [10, 101]. Glycans are attached to proteins either via the nitrogen atom of an asparagine side chain (N-glycosylation) or via the oxygen atom of threonine or serine side chains (O-glycosylation) [10]. The glycocalyx plays an important role for the cell as a physical protective barrier, and in cell morphology,

AF647 or CD58-AF647 and ZAP70mNG intensities at the contact and outside or within the cell were quantified and normalized (right). E) Lattice Light Sheet Microscopy of contact formation between GUVs decorated with pMHC/9V-AF647 or pMHC/3P9V-AF647 and ZAP70mNG expressing Jurkat T cells. Maximum intensity projection of a z-stack of a cell-GUV contact at time point 1 min 30 s (left). Time series of the cell-GUV contact in one z-plane with every 30s shown. F) Schematic representation of Jurkat T cell line loaded with fluorescent dye Fluo-4 visualizing Ca^{2+} release upon cell activation due to binding to proteins reconstituted on the GUV (right). Time series of the contact between Fluo-4 loaded Jurkat T cells and GUVs decorated with pMHC/9V-AF647 or pMHC/3P9V-AF647 in one z-plane with every 30 s shown. Superplots show individual contacts as small symbols. Large symbols depict the mean of the individual biological replicates. Symbol corresponds to the individual biological replicate (n = 3). Standard error of the mean is shown. Scale bar corresponds to 10 μm.

membrane protein diffusion, cell–cell communication, immune regulation, and cancer development [10]. In immune cell function, glycosylation can modulate protein properties or functions, or act as a ligand for carbohydrate-specific receptors such as selectins and sialic acid-binding immunoglobulin-like lectins (siglecs) [10, 101].

To further elucidate the role of the glycocalyx in immune cell contact formation, we employed lectins with defined sugar specificities in combination with our semi-artificial model system. Building on recent studies combining glycan microarray analysis with machine learning [102] and super-resolution enabled cell glycotyping [103], we examined the distribution of four lectins: (i) wheat germ agglutinin (WGA), a broadly specific lectin recognizing multiple terminal sugar residues including GlcNAc, GalNAc and sialic acid (Neu5Ac); (ii) Aleuria aurantia lectin (AAL), which specifically recognizes α-linked fucose with various linkages; (iii) Sambucus nigra-I-agglutinin (SNA), which binds α2,6-linked sialic acid (primarily sialylated LacNAc structures); and (iv) Maackia amurensis -II lectin (MAL-II), which attaches mainly to α2,3-linked sialic acid (primarily Galβ1-3GalNAc in O-glycans) (Figure 4A) [102].

Generally, lectin staining resulted in a relatively homogenous cell surface staining, interspersed with occasional larger protein clusters. Some degree of internalization was observed, especially during longer imaging periods (Figure 4B–E and Supplementary Figure S11). In Jurkat T cells, both WGA and AAL were overall enriched at the CD2-CD58 mediated contact (Figure 4B,C). SNA was neither fully enriched nor excluded from the contact with the CD2 reconstituted GUV (Figure 4D). MAL-II was excluded from the CD2-CD58-mediated contact (Figure 4E). None of the lectins bound to protein-free GUVs containing Ni-lipid, although MAL-II seldom accumulated at GUV–GUV contacts (Supplementary Figure S11). Lectin-stained cells positioned in close proximity to protein-free GUVs containing the fluorescent membrane dye Topfluor labeled PE lipid (TF-PE) did not show comparable enrichment and exclusion patterns as at the CD2-CD58 mediated contact (Supplementary Figure S11), confirming that the observed enrichment at the CD2-CD58 mediated contact was specific.

Our results suggest an accumulation of GlcNAc, GalNAc (WGA), and α-linked fucose (AAL) residues at the contact, whereas α2,6-linked sialic acid neither enriches nor is excluded (SNA), and 2,3-linked sialic acid is excluded (MAL-II). Notably, CD2 contains only a single N-linked glycosylation site, predominantly with high mannose content, which is required to stabilize the domain and ensure proper binding to CD58 [104]. As CD2 contains only a single glycosylation site and no lectin binding was observed on the GUV, we can exclude that the accumulation of WGA or AAL is due to CD2 enrichment. However, CD58 on the Jurkat cell side carries six N-linked glycosylation sites and has been described to be 44–68% carbohydrate [105]. Therefore, it is difficult to determine whether the observed accumulation or exclusion of specific sugar residues only reflects CD58-specific glycosylation patterns or also includes contributions from other glycoproteins or glycolipids present at the contact. Nonetheless, the strong exclusion of MAL-II suggests a more general exclusion of α2,3-linked sialic acid residues, as it is unlikely that CD58 is the only glycoprotein present at the contact. The observed enrichment of fucose residues at the contact could also reflect the accumulation of TCRs at the contact site. TCRs are highly core-fucosylated, a modification known to be important for T cell activation [106, 107].

Lectin binding to the glycosylated surface proteins increases their overall size and could lead to steric interference in contact formation and a subsequent exclusion from the contact site. Therefore, it remains unclear if MAL-II exclusion was observed due to the exclusion of α2,3-linked sialic acid residues or due to size. Another important factor to consider is the valency of the lectins employed. WGA, AAL and MAL-II are dimers [108–110], and SNA is a tetramer [111]. Multivalent lectins can bind multiple sugar residues on a single protein scaffold or can bind single sugar residues on different proteins and thereby lead to cross-linking of glycosylated proteins [112]. Furthermore, valency influences binding affinity [113]. Therefore, the employed lectins can cross-link and cluster glycosylated proteins on the Jurkat T cell surface and through that may also trigger endocytosis [114, 115], which potentially influences our quantification results and explains the observed internalization. Although further investigations employing click chemistry for specific sugar labeling [116], advanced microscopy techniques such as Lectin-PAINT [103], or omics approaches like glycoproteomics [117] are needed to fully elucidate the role of the glycocalyx at immune cell contact sites, we demonstrate that our system is suitable not only for studying the protein components of contact formation, but also to investigate the influence of the glycocalyx.

4 | Conclusion

The mechanisms governing cell–cell interfaces have long been and continue to be a central focus in biology. Thereby, especially our understanding of immune cell contacts has greatly benefited from the use of model membrane systems. The reduced complexity of such systems enables the study of individual components from lipids and proteins to glycocalyx, within a live-cell context. Here, we established both fully artificial and semi-artificial model systems based on GUVs to mimic freestanding 3D cell–cell interfaces. While we primarily explored T cell contacts, the system can be easily adapted to investigate similarities or differences of immune cell contacts formed by other lymphocytes or phagocytes. It may also be applied to investigate differences between immune cell subsets, for example, T memory versus T regulatory cells, or across cell lines, as for example Jurkat T cell immune synapses differ in topology, actin architecture, and adhesion molecule expression [118, 119]. The established semi-artificial model system could also expand the synthetic biology toolbox, for example, in immunotherapy using CAR T cells [120, 121]. It could be applied to investigate CAR T cell binding, activation or inhibition, proliferation and exhaustion in response to specific proteins or glycocalyx components reconstituted on the GUVs or the biophysical properties of the membrane. Importantly, this system is not limited to immune cell contacts and could be applied to mimic any type of cell–cell interface.

Mechanistically, we have shown that the semi-artificial model system can distinguish peptides of different affinity presented by the same MHC class I. It would be of interest to apply this system to a broader array of peptides, including both low- and high-affinity epitopes, to investigate their potential to induce

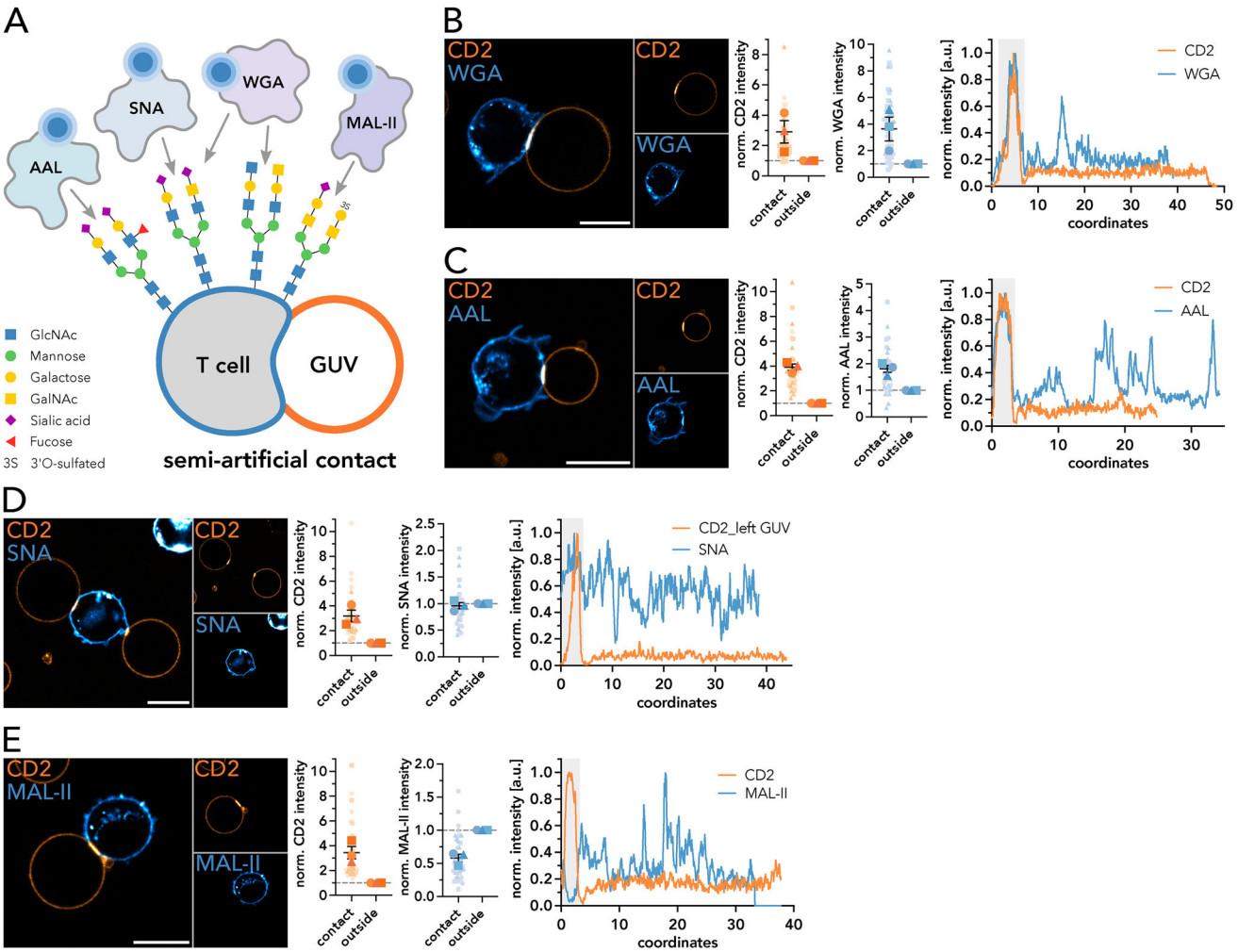

FIGURE 4 | Lectins distribute differentially at the CD2-CD58 mediated T cell-GUV contact. A) Schematic representation of the lectins used (AAL, SNA, WGA, MAL-II) to target different glycosylation patterns in the T cell glycocalyx and their distribution at the T cell GUV contact. B-E) Representative confocal image of contact formation between GUVs decorated with CD2 with Jurkat T cells labeled with WGA (B), AAL (C), SNA (D) and MAL-II (E) (left). CD2-AF488 intensity and WGA-AF647, AAL-AF647, SNA-AF647 or MAL-II-AF647 intensities at the contact and outside were quantified and normalized (middle). Linearized fluorescence intensity profiles of the GUV and cell stained with the respective lectin in the confocal image with the contact highlighted in grey (right). Superplots show individual contacts as small symbols. Large symbols depict the mean of the individual biological replicates. Symbol corresponds to the individual biological replicate (n = 3). Standard error of the mean is shown. Scale bar corresponds to 10 µm.

agonist or non-agonist interactions with the TCR. The model systems presented here could also be employed to investigate *cis* protein interactions and their potential impact on *trans* protein interactions. For example, it was reported that PD-L1 and CD80 dimerize in *cis*, which inhibits *trans* CD80:CTLA-4 and PD-L1:PD1 interactions while still maintaining *trans* CD80:CD28 engagement [122]. To investigate the size-dependent segregation observed for CD45, CD43, and MUC1 in more detail, DNA oligos of varying length attached to lipids could be applied to systematically tune the interface gap [123, 124]. In fact, a previous study employed DNA oligos reconstituted on model membranes to study the APC-T cell interface. Thereby, short DNA oligos increased T cell activation, accompanied by CD45 exclusion, while long DNA oligos hindered T cell activation with no CD45 exclusion [125]. Beyond protein distribution, we have briefly explored glycocalyx distribution at Jurkat T cell contacts using lectins. Often underestimated, the glycocalyx has immunomodulatory functions and plays an important role in cancer immune evasion [10]. While we cannot yet draw definitive conclusions regarding the enrichment or exclusion of specific sugar residues, the results highlight both the knowledge gap regarding glycocalyx influence at immune cell contacts, as well as the wide applicability of these model systems.

Further, these model systems can be used to investigate the influence of lipids on contact formation and protein distribution. Here, we have employed simple POPC membranes; however, examination of lipid compositions of varying membrane fluidity or with the ability to phase separate is of interest, as immune cell surface proteins have been shown to preferentially partition into distinct lipid environments at the contact interface [126, 127]. Measuring membrane fluidity using environment-sensitive probes [128] at the semi-artificial contact could further elucidate the role of lipids at cell–cell interfaces. In fact, decreasing membrane fluidity following granzyme and perforin release at the immune synapse has been proposed as a protective mechanism

for T and NK cells, preventing accidental death [129, 130]. Similarly, exposure of negatively charged phosphatidylserine on the outer T cell leaflet sequesters and inactivates perforin [130]. This protection mechanism could be studied in more detail using our model systems. Of note, dehydration effects might occur at membranes in close proximity, potentially affecting diffusivity and distribution of lipids in the membrane, thereby altering the membrane properties and possibly influencing the protein–protein interactions [131, 132]. The diffusion of lipids, proteins and glycocalyx components impacts their distribution and signaling at cell–cell interfaces. A major advantage of the freestanding model systems is that macromolecules are free to diffuse, allowing their dynamics to be quantified, using fluorescence (cross-) correlation spectroscopy.

While these model systems offer many advantages, they also have certain limitations. GUVs do not reflect the full complexity of a cell in terms of lipid-, protein- and glycocalyx diversity and lack an associated cytoskeleton. Although ECD size heavily influences diffusion behavior and partitioning into different lipid domains [133], full-length proteins may behave differently, potentially experiencing steric confinement that affects their distribution at the cell–cell interface. This limitation could be overcome by functionalizing GUVs with full-length transmembrane proteins [134]. Further, imaging of the free-standing reconstituted cell contacts cannot be performed using TIRF, the method of choice for 2D SLB-cell interfaces. Nonetheless, fast volumetric imaging using LLSM of the freestanding contact is feasible, enabling the visualization of cell protrusions and their pushing and pulling of the GUV membranes.

Taken together, we established two widely applicable cell–cell interface reconstitution model systems based on GUVs (artificial or semi-artificial), which form freestanding 3D contacts. These systems are highly versatile, enabling the study of any cell–cell interface in the context of lipids, proteins, and glycocalyx components.

Author Contributions

Conceptualization: F.R, A.A., E.S.; Data curation: F.R.; Methodology: F.R., R.S., X.H., E.J., A.A., L.A., E.S.; Formal analysis: F.R., A.M.S, E.S., R.S., X.H., L.A.; Funding acquisition: E.S.; Investigation: F.R., A.M.S, E.S., R.S., X.H., E.J., L.A.; Project administration: A.A., E.S.; Resources: R.S., X.H., M.D., A.A., E.S.; Software: F.R., L.A.; Supervision: F.R., M.D., E.S.; Validation: F.R., A.M.S, E.S., R.S., X.H., E.J., A.A., L.A.; Visualization: F.R.; Writing – original draft: F.R.; Writing – review & editing: A.A., R.S., E.S., E.S.

Acknowledgements

We thank the SciLifeLab Advanced Light Microscopy facility and National Microscopy Infrastructure (VR-RFI 2016-00968) for their support in imaging. We would like to thank Carolyn Shurer for kindly providing MUC1-Alexa Fluor 488 and Quentin Sattentau and Linnea Drexhage for providing the CEM cells expressing Halo-CD43-SNAP. We have been supported by Swedish Research Council Grants (grant no. 2020–02682, 2024–02993 and 2024-00289), Wellcome Leap's Dynamic Resilience Program (jointly funded by Temasek Trust), Karolinska Institutet (2024-03250; 2024–03341; 2022-00803; 2020-00997), Cancer Research KI (2024-03488), Human Frontier Science Program (RGP0025/2022), Longevity Impetus Grant from Norn Group, Hevolution Foundation and Rosenkranz Foundation. ES is an EMBO Young Investigator (YIP-2025). The Achour research group received financial support from Vetenskapsrådet (2021-05061), Cancerfonden (24 3775 Pj), Radiumhemmets Forskningsfonder (244092) and Insamlingsstiftelsen Cancer- och Allergifonden (244092).

Conflicts of Interest

The authors declare no conflict of interest.

Data Availability Statement

The data that support the findings of this study are openly available in Figshare at https://doi.org/10.17044/scilifelab.30540932 reference number 30540932.

References

1. A. Nair, P. Chauhan, B. Saha, and K. F. Kubatzky, "Conceptual Evolution of Cell Signaling," *International Journal of Molecular Sciences* 20 (2019): 3292.

2. H. E. Grecco, M. Schmick, and P. I. H. Bastiaens, "Signaling From the Living Plasma Membrane," *Cell* 144 (2011): 897–909.

3. E. Sezgin, I. Levental, S. Mayor, and C. Eggeling, "The mystery of membrane organization: Composition, regulation and roles of lipid rafts," *Nature Reviews Molecular Cell Biology* 18 (2017): 361–374.

4. M. L. Dustin, "The Immunological Synapse," *Cancer immunology research* 2 (2014): 1023–1033.

5. C. R. F. Monks, B. A. Freiberg, H. Kupfer, N. Sciaky, and A. Kupfer, "Three-dimensional segregation of supramolecular activation clusters in T cells," *Nature* 395 (1998): 82–86.

6. P. F. Céspedes, D. Beckers, M. L. Dustin, and E. Sezgin, "Model membrane systems to reconstitute immune cell signaling," *The FEBS Journal* 288 (2021): 1070–1090.

7. T. W. McKeithan, "Kinetic proofreading in T-cell receptor signal transduction," *Proceedings of the National Academy of Sciences* 92 (1995): 5042–5046.

8. W. Cho and R. V. Stahelin, "Membrane-protein interactions in cell signaling and membrane trafficking," *Annual Review of Biophysics* 34 (2005): 119–151.

9. M. A. Lemmon, "Membrane recognition by phospholipid-binding domains," *Nature Reviews Molecular Cell Biology* 9 (2008): 99–111.

10. L. Möckl, "The emerging role of the mammalian glycocalyx in functional membrane organization and immune system regulation," *Frontiers in Cell and Developmental Biology* 8 (2020): 253.

11. A. T. Ritter, K. L. Angus, and G. M. Griffiths, "The role of the cytoskeleton at the immunological synapse," *Immunological Reviews* 256 (2013): 107–117.

12. G. Bertolet and D. Liu, *Natural Killer Cells: Methods and Protocols*, ed. S. S. Somanchi, (Springer, 2016), 151–165.

13. M. L. Dustin, T. Starr, R. Varma, and V. K. Thomas, "Supported Planar Bilayers for Study of the Immunological Synapse," *Current Protocols in Immunology* 76 (2007): 18131.

14. A. Grakoui, S. K. Bromley, C. Sumen, et al., "The Immunological Synapse: A Molecular Machine Controlling T Cell Activation," *Science* 285 (1999): 221–227.

15. K. G. Johnson, S. K. Bromley, M. L. Dustin, and M. L. Thomas, "A supramolecular basis for CD45 tyrosine phosphatase regulation in sustained T cell activation," *Proceedings of the National Academy of Sciences* 97 (2000): 10138–10143.

16. F. B. Lopes, Š. Bálint, S. Valvo, et al., "Membrane nanoclusters of FcγRI segregate From inhibitory SIRPα upon activation of human macrophages," *Journal of Cell Biology* 216 (2017): 1123–1141.

17. M. Brameshuber, E. Klotzsch, A. Ponjavic, and E. Sezgin, "Understanding immune signaling using advanced imaging techniques," *Biochemical Society Transactions* 50 (2022): 853–866.

18. D. Beckers, D. Urbancic, and E. Sezgin, "Impact of Nanoscale Hindrances on the Relationship Between Lipid Packing and Diffusion in Model Membranes," *The Journal of Physical Chemistry B* 124 (2020): 1487–1494.

19. E. Sezgin and P. Schwille, "Model membrane platforms to study protein-membrane interactions," *Molecular Membrane Biology* 29 (2012): 144–154.

20. N. Bufi, M. Saitakis, S. Dogniaux, et al., "Human Primary Immune Cells Exhibit Distinct Mechanical Properties that Are Modified by Inflammation," *Biophysical Journal* 108 (2015): 2181–2190.

21. A. H. Lippert, I. B. Dimov, A. K. Winkel, et al., "Soft Polydimethylsiloxane-Supported Lipid Bilayers for Studying T Cell Interactions," *Biophysical Journal* 120 (2021): 35–45.

22. W. Jin, F. Tamzalit, P. K. Chaudhuri, C. T. Black, M. Huse, and L. C. Kam, "T cell activation and immune synapse organization respond to the microscale mechanics of structured surfaces," *Proceedings of the National Academy of Sciences* 116 (2019): 19835–19840.

23. E. Judokusumo, E. Tabdanov, S. Kumari, M. L. Dustin, and L. C. Kam, "Mechanosensing in T lymphocyte activation," *Biophysical Journal* 102 (2012): pL5–L7.

24. L. H. Lambert, G. K. E. Goebrecht, S. E. De Leo, et al., "Improving T Cell Expansion With a Soft Touch," *Nano Letters* 17 (2017): 821–826.

25. F. S. Majedi, M. M. Hasani-Sadrabadi, T. J. Thauland, S. Li, L.-S. Bouchard, and M. J. Butte, "T-cell activation is modulated by the 3D mechanical microenvironment," *Biomaterials* 252 (2020): 120058.

26. M. Saitakis, S. Dogniaux, C. Goudot, et al., "Different TCR-induced T lymphocyte responses are potentiated by stiffness with variable sensitivity," *Elife* 6 (2017): 23190.

27. S. Shaheen, Z. Wan, Z. Li, et al., "Substrate stiffness governs the initiation of B cell activation by the concerted signaling of PKCβ and focal adhesion kinase," *Elife* 6 (2017): 23060.

28. Y. Zeng, J. Yi, Z. Wan, et al., "Substrate stiffness regulates B-cell activation, proliferation, class switch, and T-cell-independent antibody responses in vivo," *European Journal of Immunology* 45 (2015): 1621–1634.

29. R. Glazier and K. Salaita, "Supported lipid bilayer platforms to probe cell mechanobiology," *Biochimica Et Biophysica Acta* 1859 (2017): 1465–1482.

30. S. F. Fenz and K. Sengupta, "Giant vesicles as cell models," *Integr Biol (Camb)* 4 (2012): 982–995.

31. N. F. Morales-Penningston, J. Wu, E. R. Farkas, et al., "GUV preparation and imaging: Minimizing artifacts," *Biochimica et Biophysica Acta (BBA)—Biomembranes* 1798 (2010): 1324–1332.

32. E. M. Schmid, D. L. Richmond, and D. A. Fletcher, *Methods in Cell Biology*, ed. J. Ross, (Academic Press, 2015), 319–338.

33. C. B. Carbone, N. Kern, R. A. Fernandes, et al., "In vitro reconstitution of T cell receptor-mediated segregation of the CD45 phosphatase," *Proceedings of the National Academy of Sciences* 114 (2017): E9338.

34. E. M. Schmid, M. H. Bakalar, K. Choudhuri, et al., "Size-dependent protein segregation at membrane interfaces," *Nature Physics* 12 (2016): 704–711.

35. E. Jenkins, A. M. Santos, C. O'Brien-Ball, et al., "Reconstitution of immune cell interactions in free-standing membranes," *Journal of Cell Science* 132 (2019): jcs219709.

36. D. I. Danylchuk, S. Moon, K. Xu, and A. S. Klymchenko, "Switchable Solvatochromic Probes for Live-Cell Super-resolution Imaging of Plasma Membrane Organization," *Angewandte Chemie* 131 (2019): 15062–15066.

37. A. Achour, J. Michaëlsson, R. A. Harris, et al., "A Structural Basis for LCMV Immune Evasion," *Immunity* 17 (2002): 757–768.

38. A. D. Duru, R. Sun, E. B. Allerbring, et al., "Tuning antiviral CD8 T-cell response via proline-altered peptide ligand vaccination," *PLOS Pathogens* 16 (2020): 1008244.

39. J.-L. Chen, G. Stewart-Jones, G. Bossi, et al., "Structural and kinetic basis for heightened immunogenicity of T cell vaccines," *The Journal of Experimental Medicine* 201 (2005): 1243–1255.

40. A. Achour, R. A. Harris, K. Persson, et al., "Murine class I major histocompatibility complex H–2D d: Expression, refolding and crystallization," *Acta Crystallographica Section D Biological Crystallography* 55 (1999): 260–262.

41. E. Sezgin, H.-J. Kaiser, T. Baumgart, P. Schwille, K. Simons, and I. Levental, "Elucidating membrane structure and protein behavior using giant plasma membrane vesicles," *Nature Protocols* 7 (2012): 1042–1051.

42. E. Sezgin, I. Levental, M. Grzybek, et al., "Partitioning, diffusion, and ligand binding of raft lipid analogs in model and cellular plasma membranes," *Biochimica et Biophysica Acta (BBA)—Biomembranes* 1818 (2012): 1777–1784.

43. L. Z. Drexhage, S. Zhang, M. Dupont, et al., "Apoptosis-mediated ADAM10 activation removes a mucin barrier promoting T cell efferocytosis," *Nature Communications* 15 (2024): 541.

44. J. Schindelin, I. Arganda-Carreras, E. Frise, et al., "Fiji: An open-source platform for biological-image analysis," *Nature Methods* 9 (2012): 676–682.

45. F. Weber, S. Iskrak, F. Ragaller, et al., "VISION – an open-source software for automated multi-dimensional image analysis of cellular biophysics," *Journal of Cell Science* 137 (2024): jcs262166.

46. T. A. Springer, "Adhesion receptors of the immune system," *Nature* 346 (1990): 425–434.

47. J. M. Boulter, N. Schmitz, A. K. Sewell, A. J. Godkin, M. F. Bachmann, and A. M. Gallimore, "Potent T cell agonism mediated by a very rapid TCR/pMHC interaction," *European Journal of Immunology* 37 (2007): 798–806.

48. M. F. Krummel and J. P. Allison, "CD28 and CTLA-4 have opposing effects on the response of T cells to stimulation," *The Journal of experimental medicine* 182 (1995): 459–465.

49. J. L. Riley, "PD-1 signaling in primary T cells," *Immunological Reviews* 229 (2009): 114–125.

50. Q. Yan, V. N. Malashkevich, A. Fedorov, et al., "Structure of CD84 provides insight Into SLAM family function," *Proceedings of the National Academy of Sciences* 104 (2007): 10583–10588.

51. M.-C. Zhong and A. Veillette, "Control of T Lymphocyte Signaling by Ly108, a Signaling Lymphocytic Activation Molecule Family Receptor Implicated in Autoimmunity," *Journal of Biological Chemistry* 283 (2008): 19255–19264.

52. Y. Gartshteyn, A. D. Askanase, R. Song, et al., "SLAMF6 compartmentalization enhances T cell functions," *Life Sci Alliance* 6 (2022): 202201533.

53. E. Hajaj, G. Eisenberg, S. Klein, et al., "SLAMF6 deficiency augments tumor killing and skews Toward an effector phenotype revealing it as a novel T cell checkpoint," *Elife* 9 (2020): 52539.

54. P. A. Valdez, H. Wang, D. Seshasayee, et al., "NTB-A, a New Activating Receptor in T Cells That Regulates Autoimmune Disease," *Journal of Biological Chemistry* 279 (2004): 18662–18669.

55. M. Cuenca, J. Sintes, Á. Lányi, and P. Engel, "CD84 cell surface signaling molecule: An emerging biomarker and target for cancer and autoimmune disorders," *Clinical Immunology* 204 (2019): 43–49.

56. J. Steinkühler, E. Sezgin, I. Urbančič, C. Eggeling, and R. Dimova, "Mechanical properties of plasma membrane vesicles correlate with lipid order, viscosity and cell density," *Communications Biology* 2 (2019): 337.

57. R. Varma, G. Campi, T. Yokosuka, T. Saito, and M. L. Dustin, "T Cell Receptor-Proximal Signals Are Sustained in Peripheral Microclusters and

Terminated in the Central Supramolecular Activation Cluster," *Immunity* 25 (2006): 117–127.

58. V. T. Chang, R. A. Fernandes, K. A. Ganzinger, et al., "Initiation of T cell signaling by CD45 segregation at 'close contacts'," *Nature Immunology* 17 (2016): 574–582.

59. Y. Jung, L. Wen, A. Altman, and K. Ley, "CD45 pre-exclusion From the tips of T cell microvilli prior to antigen recognition," *Nature Communications* 12 (2021): 3872.

60. S. J. Davis and P. A. van der Merwe, "The structure and ligand interactions of CD2: Implications for T-cell function," *Immunology Today* 17 (1996): 177–187.

61. L. A. Earl and L. G. Baum, "CD45 Glycosylation controls T-cell life and death," *Immunology & Cell Biology* 86 (2008): 608–615.

62. B. Ardman, M. A. Sikorski, and D. E. Staunton, "CD43 interferes With T-lymphocyte adhesion," *Proceedings of the National Academy of Sciences* 89 (1992): 5001–5005.

63. J. G. Cyster, D. M. Shotton, and A. F. Williams, "The dimensions of the T lymphocyte glycoprotein leukosialin and identification of linear protein epitopes that can be modified by glycosylation," *The EMBO Journal* 10 (1991): 893–902.

64. C. L. Hattrup and S. J. Gendler, "Structure and Function of the Cell Surface (Tethered) Mucins," *Annual Review of Physiology* 70 (2008): 431–457.

65. J. P. M. van Putten and K. Strijbis, "Transmembrane Mucins: Signaling Receptors at the Intersection of Inflammation and Cancer," *Journal of Innate Immunity* 9 (2017): 281–299.

66. A. Bretscher, "Regulation of cortical structure by the ezrin-radixin-moesin protein family," *Current Opinion in Cell Biology* 11 (1999): 109–116.

67. S. Yonemura, M. Hirao, Y. Doi, et al., "Ezrin/Radixin/Moesin (ERM) Proteins Bind to a Positively Charged Amino Acid Cluster in the Juxta-Membrane Cytoplasmic Domain of CD44, CD43, and ICAM-2," *The Journal of Cell Biology* 140 (1998): 885–895.

68. E. J. Allenspach, P. Cullinan, J. Tong, et al., "ERM-Dependent Movement of CD43 Defines a Novel Protein Complex Distal to the Immunological Synapse," *Immunity* 15 (2001): 739–750.

69. J. Tong, E. J. Allenspach, S. M. Takahashi, et al., "CD43 Regulation of T Cell Activation Is Not Through Steric Inhibition of T Cell–APC Interactions but Through an Intracellular Mechanism," *The Journal of Experimental Medicine* 199 (2004): 1277–1283.

70. B. Agrawal, N. Gupta, and J. D. Konowalchuk, "MUC1 Mucin: A Putative Regulatory (Checkpoint) Molecule of T Cells," *Frontiers in Immunology* 9 (2018): 2391.

71. S. Mahanta, S. P. Fessler, J. Park, and C. Bamdad, "A Minimal Fragment of MUC1 Mediates Growth of Cancer Cells," *PLoS ONE* 3 (2008): 2054.

72. K. E. Haugstad, T. A. Gerken, B. T. Stokke, T. K. Dam, C. F. Brewer, and M. Sletmoen, "Enhanced Self-Association of Mucins Possessing the T and Tn Carbohydrate Cancer Antigens at the Single-Molecule Level," *Biomacromolecules* 13 (2012): 1400–1409.

73. G. Misevic and E. Garbarino, "Glycan-to-Glycan Binding: Molecular Recognition Through Polyvalent Interactions Mediates Specific Cell Adhesion," *Molecules (Basel, Switzerland)* 26 (2021): 397.

74. C. S. Brandt, M. Baratin, E. C. Yi, et al., "The B7 family member B7-H6 is a tumor cell ligand for the activating natural killer cell receptor NKp30 in humans," *Journal of Experimental Medicine* 206 (2009): 1495–1503.

75. T. O. J. Cockram, J. M. Dundee, A. S. Popescu, and G. C. Brown, "The Phagocytic Code Regulating Phagocytosis of Mammalian Cells," *Frontiers in Immunology* 12 (2021): 629979.

76. S. Freeman and S. Grinstein, "Promoters and Antagonists of Phagocytosis: A Plastic and Tunable Response," *Annual Review of Cell and Developmental Biology* 37 (2021): 89–114.

77. Y. Zhang, Q. Liu, S. Yang, and Q. Liao, "CD58 Immunobiology at a Glance," *Frontiers in Immunology* 12 (2021): 705260.

78. D. Depoil, S. Fleire, B. L. Treanor, et al., "CD19 is essential for B cell activation by promoting B cell receptor–antigen microcluster formation in response to membrane-bound ligand," *Nature Immunology* 9 (2008): 63–72.

79. M. H. Bakalar, A. M. Joffe, E. M. Schmid, S. Son, M. Podolski, and D. A. Fletcher, "Size-Dependent Segregation Controls Macrophage Phagocytosis of Antibody-Opsonized Targets," *Cell* 174 (2018): 131–142.e13.

80. J. H. Felce, E. Sezgin, M. Wane, et al., "CD45 exclusion– and cross-linking–based receptor signaling together broaden FcεRI reactivity," *Science Signaling* 11 (2018): 17.

81. D.-H. Wi, J.-H. Cha, and Y.-S. Jung, "Mucin in cancer: A stealth cloak for cancer cells," *BMB Reports* 54 (2021): 344–355.

82. K. Zhang, R. Sikut, and G. C. Hansson, "A MUC1 Mucin Secreted From a Colon Carcinoma Cell Line Inhibits Target Cell Lysis by Natural Killer Cells," *Cellular Immunology* 176 (1997): 158–165.

83. L. Li, L. Yang, and D. Jiang, "Research progress of CD80 in the development of immunotherapy drugs," *Frontiers in immunology* 15 (2024): 1496992.

84. A. Legat, D. E. Speiser, H. Pircher, D. Zehn, and S. A. Fuertes Marraco, "Inhibitory Receptor Expression Depends More Dominantly on Differentiation and Activation than "Exhaustion" of Human CD8 T Cells," *Frontiers in immunology* 4 (2013): 455.

85. Y. Li and R. J. Kurlander, "Comparison of anti-CD3 and anti-CD28-coated beads With soluble anti-CD3 for expanding human T cells: Differing impact on CD8 T cell phenotype and responsiveness to restimulation," *Journal of Translational Medicine* 8 (2010): 104.

86. S. K. Bromley, A. Iaboni, S. J. Davis, et al., "The immunological synapse and CD28-CD80 interactions," *Nature Immunology* 2 (2001): 1159–1166.

87. N. Beyersdorf, T. Kerkau, and T. Hünig, "CD28 co-stimulation in T-cell homeostasis: A recent perspective," *ImmunoTargets and therapy* 4 (2015): 111.

88. M. Chatterjee, K. Kis-Toth, T.-H. Thai, C. Terhorst, and G. C. Tsokos, "SLAMF6-driven co-stimulation of human peripheral T cells is defective in SLE T cells," *Autoimmunity* 44 (2011): 211–218.

89. B. Monel, P. A. Lamothe, J. Meyo, et al., "SLAMF6 enables efficient attachment, synapse formation, and killing of HIV-1-infected $CD4^+$ T cells by virus-specific $CD8^+$ T cells," *BioRxiv* (2025).

90. S. G. Tangye, K. E. Nichols, N. J. Hare, and B. C. M. van de Weerdt, "Functional Requirements for Interactions Between CD84 and Src Homology 2 Domain-Containing Proteins and Their Contribution to Human T Cell Activation," *The Journal of Immunology* 171 (2003): 2485–2495.

91. M. A. Dragovich, K. Adam, M. Strazza, A. S. Tocheva, M. Peled, and A. Mor, "SLAMF6 clustering is required to augment T cell activation," *PLoS ONE* 14 (2019): 0218109.

92. M. Dragovich and A. Mor, "The SLAM family receptors: Potential therapeutic targets for inflammatory and autoimmune diseases," *Autoimmunity Reviews* 17 (2018): 674–682.

93. J. R. James and R. D. Vale, "Biophysical mechanism of T-cell receptor triggering in a reconstituted system," *Nature* 487 (2012): 64–69.

94. S. J. Davis and P. A. van der Merwe, "The kinetic-segregation model: TCR triggering and Beyond," *Nature Immunology* 7 (2006): 803–809.

95. K. Choudhuri, D. Wiseman, M. H. Brown, K. Gould, and P. A. van der Merwe, "T-cell receptor triggering is critically dependent on the dimensions of its peptide-MHC ligand," *Nature* 436 (2005): 578–582.

96. S.-P. Cordoba, K. Choudhuri, H. Zhang, et al., "The large ectodomains of CD45 and CD148 regulate their segregation From and inhibition of ligated T-cell receptor," *Blood* 121 (2013): 4295–4302.

97. S. C. Bunnell, D. I. Hong, J. R. Kardon, et al., "T cell receptor ligation induces the formation of dynamically regulated signaling assemblies," *The Journal of Cell Biology* 158 (2002): 1263–1275.

98. G. Campi, R. Varma, and M. L. Dustin, "Actin and agonist MHC–peptide complex–dependent T cell receptor microclusters as scaffolds for signaling," *The Journal of Experimental Medicine* 202 (2005): 1031–1036.

99. C. Binder, F. Cvetkovski, F. Sellberg, et al., "CD2 Immunobiology," *Frontiers in immunology* 11 (2020): 1090.

100. B.-C. Chen, W. R. Legant, K. Wang, et al., "Lattice light-sheet microscopy: Imaging molecules to embryos at high spatiotemporal resolution," *Science* 346 (2014): 1257998.

101. B. A. H. Smith and C. R. Bertozzi, "The clinical impact of glycobiology: Targeting selectins, Siglecs and mammalian glycans," *Nature Reviews Drug Discovery* 20 (2021): 217–243.

102. D. Bojar, L. Meche, G. Meng, et al., "A Useful Guide to Lectin Binding: Machine-Learning Directed Annotation of 57 Unique Lectin Specificities," *ACS Chemical Biology* 17 (2022): 2993–3012.

103. M. M. E. Tholen, R. Riera, C. Izquierdo-Lozano, and L. Albertazzi, "Multiplexed Lectin-PAINT super-resolution microscopy enables cell glycotyping," *Communications Biology* 8 (2025): 267.

104. M. A. Recny, M. A. Luther, M. H. Knoppers, et al., "N-glycosylation is required for human CD2 immunoadhesion functions," *Journal of Biological Chemistry* 267 (1992): 22428–22434.

105. B. P. Wallner, A. Z. Frey, R. Tizard, et al., "Primary structure of lymphocyte function-associated antigen 3 (LFA-3). The ligand of the T lymphocyte CD2 glycoprotein," *The Journal of experimental medicine* 166 (1987): 923–932.

106. H. Fujii, S. Shinzaki, H. Iijima, et al., "Core Fucosylation on T Cells, Required for Activation of T-Cell Receptor Signaling and Induction of Colitis in Mice, Is Increased in Patients With Inflammatory Bowel Disease," *Gastroenterology* 150 (2016): 1620–1632.

107. W. Liang, S. Mao, S. Sun, et al., "Core Fucosylation of the T Cell Receptor Is Required for T Cell Activation," *Frontiers in immunology* 9 (2018): 78.

108. G. K. B S and A. Surolia, "Comprehensive analysis of α 2–3-linked sialic acid specific Maackia amurensis leukagglutinin reveals differentially occupied N -glycans and C-terminal processing," *International Journal of Biological Macromolecules* 94 (2017): 114–121.

109. J. Olausson, E. Åström, B.-H. Jonsson, L. A. E. Tibell, and P. Påhlsson, "Production and characterization of a monomeric form and a single-site form of Aleuria aurantia lectin," *Glycobiology* 21 (2011): 34–44.

110. M. del Carmen Portillo-Téllez, M. Bello, G. Salcedo, G. Gutiérrez, V. Gómez-Vidales, and E. García-Hernández, "Folding and Homodimerization of Wheat Germ Agglutinin," *Biophysical Journal* 101 (2011): 1423–1431.

111. N. Shibuya, I. J. Goldstein, W. F. Broekaert, M. Nsimba-Lubaki, B. Peeters, and W. J. Peumans, "The elderberry (Sambucus nigra L.) bark lectin recognizes the Neu5Ac(alpha 2-6)Gal/GalNAc sequence," *Journal of Biological Chemistry* 262 (1987): 1596–1601.

112. M. L. Huang and K. Godula, "Nanoscale materials for probing the biological functions of the glycocalyx," *Glycobiology* 26 (2016): 797–803.

113. R. Riera, T. P. Hogervorst, W. Doelman, et al., "Single-molecule imaging of glycan–lectin interactions on cells With Glyco-PAINT," *Nature Chemical Biology* 17 (2021): 1281–1288.

114. P. R. Moody, E. J. Sayers, J. P. Magnusson, et al., "Receptor Crosslinking: A General Method to Trigger Internalization and Lysosomal Targeting of Therapeutic Receptor:Ligand Complexes," *Molecular Therapy* 23 (2015): 1888–1898.

115. D. Paul, O. Stern, Y. Vallis, J. Dhillon, A. Buchanan, and H. McMahon, "Cell surface protein aggregation triggers endocytosis to maintain plasma membrane proteostasis," *Nature Communications* 14 (2023): 947.

116. J. C. Jewett, E. M. Sletten, and C. R. Bertozzi, "Rapid Cu-Free Click Chemistry With Readily Synthesized Biarylazacyclooctynones," *Journal of the American Chemical Society* 132 (2010): 3688–3690.

117. C. M. Woo, A. Felix, W. E. Byrd, et al., "Development of IsoTaG, a Chemical Glycoproteomics Technique for Profiling Intact N- and O-Glycopeptides From Whole Cell Proteomes," *Journal of Proteome Research* 16 (2017): 1706–1718.

118. C. Cassioli, S. Balint, E. B. Compeer, et al., "Increasing LFA-1 Expression Enhances Immune Synapse Architecture and T Cell Receptor Signaling in Jurkat E6.1 Cells," *Frontiers in Cell and Developmental Biology* 9 (2021): 673446.

119. S. Kumari, H. Colin-York, D. J. Irvine, and M. Fritzsche, "Not All T Cell Synapses Are Built the Same Way," *Trends in Immunology* 40 (2019): 977–980.

120. G. Marsico, S. Gc, and V. Siciliano, "Synthetic Biology and Biomaterials Strategies to Deceive the Tumor Microenvironment in CAR-T Immunotherapy," *Small* 21 (2025): 06429.

121. L. Russo, I. De Martino, M. Marchetti, and V. Siciliano, "Engineered T cells and macrophages: Two arms to seize solid tumors," *Current Opinion in Biotechnology* 93 (2025): 103296.

122. Y. Zhao, C. K. Lee, C.-H. Lin, et al., "PD-L1:CD80 Cis-Heterodimer Triggers the Co-stimulatory Receptor CD28 While Repressing the Inhibitory PD-1 and CTLA-4 Pathways," *Immunity* 51 (2019): 1059–1073.

123. Y.-H. M. Chan, B. van Lengerich, and S. G. Boxer, "Effects of linker sequences on vesicle fusion mediated by lipid-anchored DNA oligonucleotides," *Proceedings of the National Academy of Sciences* 106 (2009): 979–984.

124. R. Rubio-Sánchez, G. Fabrini, P. Cicuta, and L. Di Michele, "Amphiphilic DNA nanostructures for bottom-up synthetic biology," *Chemical Communications* 57 (2021): 12725–12740.

125. Y. Du, Y. Lyu, J. Lin, et al., "Membrane-anchored DNA nanojunctions enable closer antigen-presenting cell–T-cell contact in elevated T-cell receptor triggering," *Nature Nanotechnology* 18 (2023): 818–827.

126. S. A. Shelby, I. Castello-Serrano, K. C. Wisser, I. Levental, and S. L. Veatch, "Membrane phase separation drives responsive assembly of receptor signaling domains," *Nature Chemical Biology* 19 (2023): 750–758.

127. I. Urbančič, L. Schiffelers, E. Jenkins, et al., "Aggregation and mobility of membrane proteins interplay with local lipid order in the plasma membrane of T cells," *FEBS Letters* 595 (2021): 2127–2146.

128. P. Carravilla, L. Andronico, J. Schlegel, et al., "Measuring plasma membrane fluidity using confocal microscopy," *Nature Protocols* 20 (2025): 1976–2004.

129. Y. Li and J. S. Orange, "Degranulation enhances presynaptic membrane packing, which protects NK cells from perforin-mediated autolysis," *PLoS Biology* 19 (2021): 3001328.

130. J. A. Rudd-Schmidt, A. W. Hodel, T. Noori, et al., "Lipid order and charge protect killer T cells From accidental death," *Nature Communications* 10 (2019): 5396.

131. M. Chattopadhyay, E. Krok, H. Orlikowska, P. Schwille, H. G. Franquelim, and L. Piatkowski, "Hydration Layer of Only a Few Molecules Controls Lipid Mobility in Biomimetic Membranes," *Journal of the American Chemical Society* 143 (2021): 14551–14562.

132. H. Orlikowska-Rzeznik, E. Krok, M. Domanska, et al., "Dehydration of Lipid Membranes Drives Redistribution of Cholesterol Between Lateral Domains," *The Journal of Physical Chemistry Letters* 15 (2024): 4515–4522.

133. C. O. Gurdap, L. Wedemann, T. Sych, and E. Sezgin, "Influence of the extracellular domain size on the dynamic behavior of membrane proteins," *Biophysical Journal* 121 (2022): 3826–3836.

134. M. Dezi, A. Di Cicco, P. Bassereau, and D. Lévy, "Detergent-mediated incorporation of transmembrane proteins in giant unilamellar vesicles with controlled physiological contents," *Proceedings of the National Academy of Sciences* 110 (2013): 7276–7281.

Supporting Information

Additional supporting information can be found online in the Supporting Information section.

Supporting File: advs74891-sup-0001-SuppMat.pdf.